

RESEARCH ARTICLE

10.1002/2016JD024941

Key Points:

- Similar trend but different ranges in DSD μ - λ relation between aircraft and surface measurements reveal the cloud-to-precipitation process
- Compared to the Gamma function, the Exponential function shows its validity by capturing most DSD shape information except for large drops
- The new DSD parameterization is robust, while the Q2 SR QPE based on constant DSD intercept assumption needs revision for $Z_e > 20$ dBZ

Correspondence to:

X. Dong,
dong@aero.und.edu

Citation:

Wang, J., X. Dong, B. Xi, and A. J. Heymsfield (2016), Investigation of liquid cloud microphysical properties of deep convective systems: 1. Parameterization of raindrop size distribution and its application for stratiform rain estimation, *J. Geophys. Res. Atmos.*, 121, 10,739–10,760, doi:10.1002/2016JD024941.

Received 15 FEB 2016

Accepted 9 AUG 2016

Accepted article online 13 AUG 2016

Published online 20 SEP 2016

Investigation of liquid cloud microphysical properties of deep convective systems: 1. Parameterization of raindrop size distribution and its application for stratiform rain estimation

Jingyu Wang¹, Xiquan Dong¹, Baixe Xi¹, and Andrew J. Heymsfield²
¹Department of Atmospheric Sciences, University of North Dakota, Grand Forks, North Dakota, USA, ²National Center for Atmospheric Research, Boulder, Colorado, USA

Abstract To investigate liquid-phase ($T > 3^\circ\text{C}$) cloud and precipitation microphysical properties within Deep Convective Systems (DCSs), eight DCS cases sampled by the University of North Dakota Citation II research aircraft during Midlatitude Continental Convective Clouds Experiment were selected. A full spectrum of raindrop size distribution (DSD) was constructed from $120\ \mu\text{m}$ to $4000\ \mu\text{m}$ through a combination of two-dimensional cloud probe (120 to $900\ \mu\text{m}$) and High Volume Precipitation Spectrometer (900 to $4000\ \mu\text{m}$) data sets. A total of 1126 five second DSDs have been used to fit to Gamma and Exponential functions within the stratiform rain (SR) regions of DCSs. The Gamma shape μ_T and slope λ_T parameters are then compared with those derived from surface disdrometer measurements. The similar μ_T - λ_T relationships but different μ_T and λ_T value ranges from two independent platforms at different elevations may represent the real nature of DSD shape information in clouds and at the surface. To apply the exponentially fitted DSD parameters to precipitation estimation using Next Generation Weather Radar (NEXRAD) radar reflectivity factor Z_e , the terms N_{0E} and λ_E have been parameterized as a function of Z_e using an empirical N_{0E} - λ_E relationship. The averaged SR rain rate retrieved from this study is almost identical to the surface measurements, while the NEXRAD Q2 precipitation is twice as large. The comparisons indicate that the new DSD parameterization scheme is robust, while the Q2 SR precipitation estimation based on Marshall-Palmer Z-R relationship, where a constant DSD intercept parameter (N_{0E}) was assumed, needs to be improved for heavy precipitation cases.

1. Introduction

Deep Convective Systems (DCSs) with radar echo top altitudes from $500\ \text{hPa}$ ($\sim 6\ \text{km}$) to the tropopause can be separated into a deep convective precipitating portion and a nonprecipitating anvil canopy [Feng et al., 2011, 2012]. The former dominates much of the warm season intense rainfall over the midlatitudes, while the latter plays a significant role in the atmospheric radiation budget due to its extensive spatial coverage. DCS systems strongly affect local climate and provide important feedbacks to the global climate system through their radiative effects and distribution of moisture [Futyan and Del Genio, 2007; Feng et al., 2011, 2012].

Feng et al. [2011] developed a hybrid classification method to objectively identify components of DCSs into the convective core (CC), stratiform region (SR), and anvil clouds (ACs), using a combination of ground-based (Next Generation Weather Radar, NEXRAD) and spaceborne (GOES) data. The hybrid classification algorithm builds upon a previous convective-stratiform algorithm [Steiner et al., 1995], by incorporating anvil classifications and satellite data, providing a thorough means for studying the life and diurnal cycles of DCSs, as well as their associated precipitation [Feng et al., 2012]. They also found that precipitation comes almost exclusively from the CC and SR regions of DCSs and that the probability density function (PDF) of the averaged CC rain rates (RR_{CC}) is similar to that in the SR regions (RR_{SR}), except that the magnitude of averaged RR_{CC} is 10 times higher than that of averaged RR_{SR} .

The characteristics of stratiform rainfall in DCSs have been intensively investigated through a variety of platforms, including satellite (e.g., Tropical Rainfall Measuring Mission (TRMM) precipitation radar) [Liu et al., 2007; Schumacher and Houze, 2003; Xu, 2013], ground-based radar (e.g., National Mosaic and Multi-Sensor Quantitative Precipitation Estimation, also known as NMQ or Q2) [Chen et al., 2013; Stenz et al., 2014, 2015],

surface rain gauge network (e.g., Oklahoma Mesonet observations) [Brock *et al.*, 1995], video disdrometer [Zhang *et al.*, 2001, 2003; Cao *et al.*, 2008; Cao and Zhang, 2009], and airborne remote measurements (e.g., Multichannel Cloud Radiometer [Heymsfield and Fulton, 1988] and 10 and 94 GHz airborne radars [Boudala *et al.*, 2006; Tian *et al.*, 2007]). Because aircraft in situ measurements have better collocations with radar observations and larger sample volumes than surface disdrometer measurements, aircraft can provide more accurate raindrop size distribution (DSD) information for cloud and precipitation studies. However, to the best of our knowledge, there are no precipitation retrieval methods developed through an integrative analysis of aircraft in situ, collocated radar reflectivity, and surface rain rate measurements. The goal of this study is to derive an improved DSD retrieval method for SR regions of DCSs using aircraft in situ measurements. By applying this improved DSD retrieval method to horizontally polarized radar reflectivity prior to the dual-polarization radar upgrade, regional surface precipitation estimation and in-cloud DSD data products will be generated to further understand cloud and precipitation processes in DCSs.

The DSD is one of the most important factors in the study of DCS cloud and precipitation properties, because most cloud bulk microphysical properties are determined from the retrieved or measured DSD [Sempere-Torres *et al.*, 1994, 1998; Lee *et al.*, 2004; Fan *et al.*, 2015]. In addition, the DSD bridges the transition processes from cloud to precipitation [Pruppacher and Klett, 1996; Kumjian and Prat, 2014], an area which has been widely studied through modeling collisional coalescence and breakup processes in DCSs. However, in most previous studies, the initial DSD values aloft were either fixed or simplified [McFarquhar, 2004a, 2004b]. The Department of Energy (DOE) Atmospheric Radiation Measurement (ARM) conducted a field campaign in a collaborative effort with NASA's Global Precipitation Measurement (GPM) mission Ground Validation (GV) program, the Midlatitude Continental Convective Clouds Experiment (MC3E), at the ARM Southern Great Plains (SGP, 36°36'18"N, 97°29'6"W) site from April to June 2011 [Jensen *et al.*, 2015]. The goal of MC3E was to characterize convective cloud systems, including convective initiation and updraft and downdraft dynamics, precipitation and cloud microphysics, and their environment. The campaign consisted of the most comprehensive cloud-observing infrastructure currently available in the central United States, combined with an extensive sounding array, ground-based remote sensors, aircraft in situ measurements, and updated ARM radar instrumentation.

For the DCS modeling and forecasting community, an accurate precipitation product is needed to serve as the data set for validating model output [Clark *et al.*, 2014; Fan *et al.*, 2015]. Limited by the number of surface rain gauges, the regional precipitation product is usually estimated from observations with weather surveillance radar network. The accuracy of precipitation estimation depends primarily on the choice of power-law Z - R relationships, which are literally hundreds in existence developed using different data sets for different precipitation types [Marshall and Palmer, 1948; Rosenfeld *et al.*, 1993; Nelson *et al.*, 2010; Giangrande *et al.*, 2014]. Nonetheless, those power-law Z - R relationships, even without explicit clarification, all assume DSDs following an Exponential function with the constant intercept (N_0). Since natural DSDs rarely follow Exponential functions, a fixed N_0 even further constrained the applicability of power-law Z - R relationships. Completed in 2013, the nationwide dual-polarization radar upgrade made multivariable radar observations available (e.g., differential reflectivity and specific differential phase) [Zrnich and Ryzhkov, 1999; Ryzhkov *et al.*, 2005a, 2005b; Kumjian, 2013; Zhang *et al.*, 2015], which resulted in new precipitation estimation techniques. For example, by using a three-parameter Gamma function, Bringi *et al.* [2002] proposed a DSD retrieval method with inputs of radar reflectivity, differential reflectivity (Z_{DR}), and specific differential phase (K_{DP}). In order to further reduce the degrees of freedom in the DSD estimation, the normalized Gamma function was developed [Testud *et al.*, 2001; Zhang *et al.*, 2001; Cao *et al.*, 2008; Cao and Zhang, 2009], where the DSD can fully be represented by N_w (normalized parameter) and D_0 (median volume diameter). However, more than one radar observation is still required as input.

During the MC3E campaign in 2011, precipitation estimation was still based on Z - R relationships, with the use of horizontally polarized radar reflectivity due to the lack of operationally gridded polarimetric radar observations. The commonly used National Centers for Environmental Prediction Stage IV Quantitative Precipitation Estimation product lacks necessary temporal information due to its hourly update cycle [Baldwin and Mitchell, 1998; Lin and Mitchell, 2005], while the 5 min NEXRAD Q2 product demonstrates a nonnegligible overestimation compared to surface rain gauge measurements [Stenz *et al.*, 2014]. Motivated by the demands to accurately estimate surface precipitation and in-cloud DSD, we will focus on investigating an alternative DSD parameterization scheme and its application in radar-based precipitation estimation. Further, we hope to

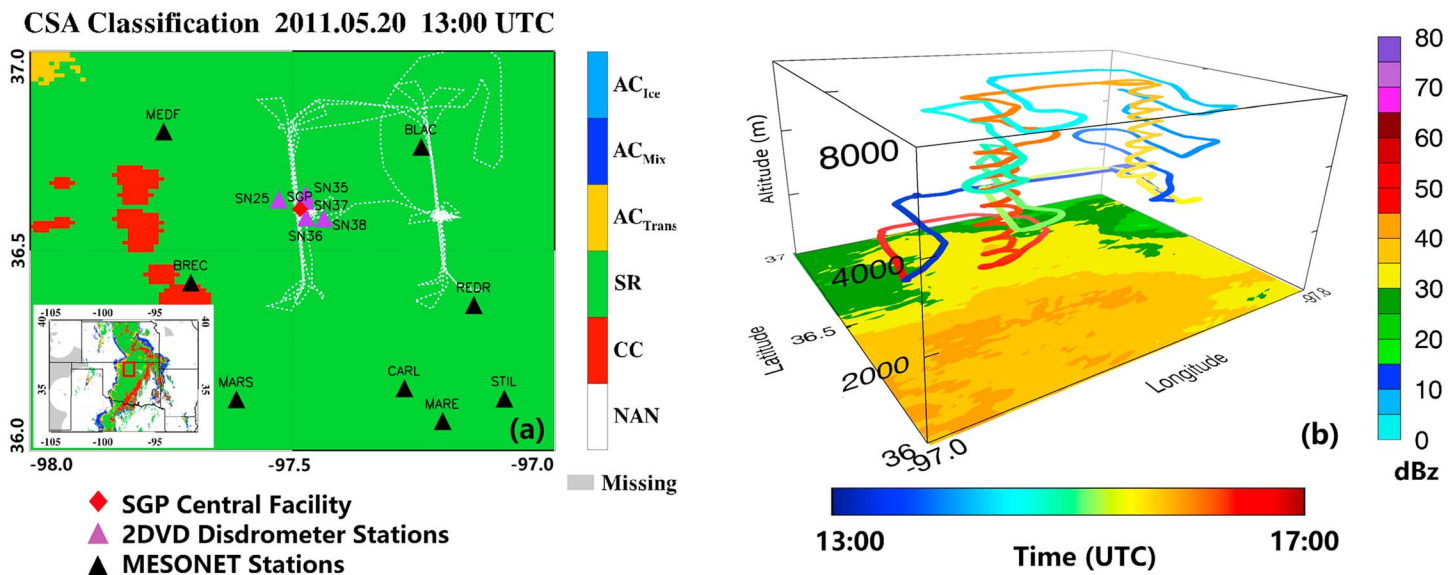


Figure 1. (a) Two-dimensional view of the flight trajectory (white dash line), ARM SGP site (red diamond), GPM GV stations (purple triangles), and Mesonet sites (black triangles) superimposed on Convective-Stratiform-Anvil (CSA) classified components (CC: Convective Core, SR: Stratiform Region, and AC: Anvil Clouds) of a Deep Convective System (DCS) on 20 May 2011. A snapshot of the entire system at one instance is shown in the left corner. (b) Similar to Figure 1a but 3-D view (the transition of aircraft trajectory from blue to red corresponds to flight time), and the XY plane represents NEXRAD radar reflectivity factors to show the horizontal variability of the DCS at an altitude of 2500 m.

better understand cloud-to-precipitation transition processes through an integrative analysis of aircraft in situ measurements in clouds and disdrometer measurements at the surface.

A total of 15 DCS cases were sampled by the University of North Dakota (UND) Citation II aircraft during MC3E, and those were categorized into ice, mixed-phase, and liquid layers [Wang *et al.*, 2015]. In this companion study, in order to develop a new DSD parameterization and retrieval scheme, eight DCS cases during MC3E were selected to investigate the liquid-phase ($T > 3^{\circ}\text{C}$) cloud and precipitation microphysical properties within DCSs. The eight selected DCS cases are 25 and 27 April and 1, 11, 18, 20, 23, and 24 May 2011, in which sufficient liquid-phase cloud samples were collected. This paper is organized as follows: Section 2 describes various data sets, including aircraft in situ measurements, ground-based NEXRAD observations, and surface rain rate measurements. Section 3 will present the newly developed DSD parameterization scheme based on aircraft in situ measurements and their application to precipitation estimation, as well as the comparison of surface rain rates among NEXRAD Q2, surface measurements, and new retrieval from this study. Finally, section 4 summarizes our findings and conclusions from this study.

2. Data

The in situ measurements of DCS microphysical properties were carried out by the UND Citation II research aircraft, which was fully equipped with state-of-the-art instruments for cloud physics research. A detailed discussion about airborne probes can be found in Wang *et al.* [2015]. The surface rain rates were measured by one Distromet model RD-80 disdrometer deployed at the ARM SGP site, five two-dimensional video disdrometers (2DVD) in the surrounding area of the ARM SGP site, and eight Mesonet tipping-bucket sensors scattered within a $1^{\circ} \times 1^{\circ}$ domain centered on the ARM SGP site (Figure 1a). In addition to these data sets, surface rain rate measurements from a total of 17 APU (Automatic Parsivel Unit) sites for the entire MC3E campaign (from 22 April to 6 June 2011) were collected and processed as an independent data set to evaluate the different Z-R relationships (a brief summary of APU stations is listed in Appendix B).

2.1. Aircraft In Situ DSD Measurements

A full spectrum of DSDs in this study was constructed from the combination of Particle Measurement System two-dimensional cloud probe (2DC, 30–3000 μm) and the SPEC Inc., High Volume Precipitation Spectrometer (HVPS, 300–30,000 μm). All DSDs collected within the liquid-phase layer of the DCSs at cloud temperatures

Equivalent Raindrop Diameter Melted from Ice Crystals

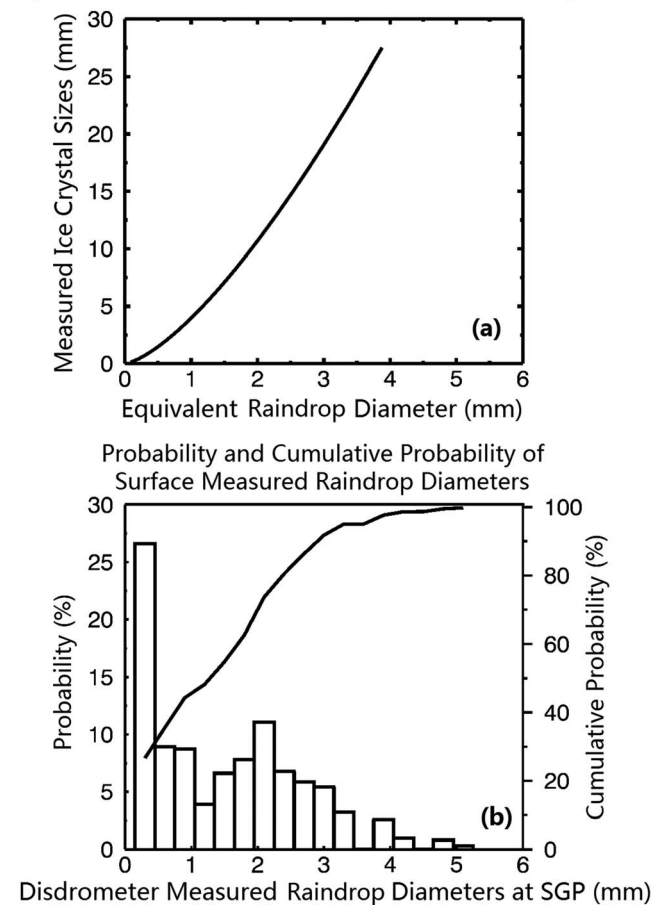


Figure 2. (a) Equivalent raindrop diameters melted from ice crystal aggregates calculated by a mass-dimensional relationship, $\text{mass} = aD^b$ where $a = 0.00365$ and $b = 2.1$ [Wang et al., 2015]. (b) Probability and cumulative probability of surface disdrometer measured raindrop diameter at the ARM SGP site.

1982b; McFarquhar and List, 1991a, 1991b; McFarquhar, 2004a, 2004b; Seifert et al., 2005; Barros et al., 2008; Schlottke et al., 2010; Emersic and Connolly, 2011], where distinct collisional breakup types were observed and parameterized, and the raindrops larger than this size could not be sustained.

By conservation of mass, using the ice mass-dimensional relationship ($\text{mass} = aD^b$, $a = 0.00365$, $b = 2.1$) established during MC3E [Wang et al., 2015], Figure 2a shows an independent investigation of possible equivalent melted diameters based on aircraft in situ measurements above the melting layer during the campaign. In other words, the majority of ice crystal aggregates above the melting layer can melt to an equivalent diameter of less than 4 mm. The 4 mm size threshold coincides with previous in situ measurements [Szumowski et al., 1997, 1998], where they concluded that the raindrops with $D > 4$ mm are more likely to be associated with strong updrafts, but also possible from melting graupel and hail outside of strong updrafts. However, we do not rule out the aggregation process within the melting layer. As demonstrated in previous studies [Barthazy et al., 1998; Tromel et al., 2014], the aggregation process can lead to larger than expected raindrops from the melting process.

In addition, this result is further confirmed by the probability of raindrop diameters measured by the ARM SGP RD-80 disdrometer as shown in Figure 2b, where most of the raindrop diameters are less than 4 mm. By considering the aircraft in situ measurements and surface disdrometer measurements, the limit of the maximum raindrop diameter is set to 4 mm in this study for the following reasons. First, there are no algorithms to date that are capable of removing all these large elongated artifacts, which are more likely

above 3°C were used in this study. The cloud properties with a range of temperatures from 0°C to 3°C were eliminated from this study mostly to rule out melting layer cases. It is important to note that no hail was reported within the study domain for the selected cases. This temperature range is consistent with the altitude of the radar bright band where ice particles fall just below the 0°C level [Fujiyoshi, 1986; Oraltay and Hallett, 2005; Heymsfield et al., 2015]. As a result, a temperature of 3°C was chosen as the criterion to distinguish liquid-phase from mixed-phase clouds.

The first three channels of the 2DC were discarded because of the issue of questions about the depth of field and errors involving the digitization of small particles [Korolev et al., 1998]. For large raindrops measured by the HVPS, elongated “artifacts” with sizes greater than 10 mm were sometimes observed, presumably due to probe errors, and were eliminated from the data set. Another important source of artifacts is the recorded splash pattern when raindrops hit the probe tips. After careful examination of the in situ measured particle images, we concluded that there are no raindrops greater than 5.5 mm within the regions sampled in this study. This conclusion is also consistent with the previous studies of breakup processes of raindrops [Low and List, 1982a,

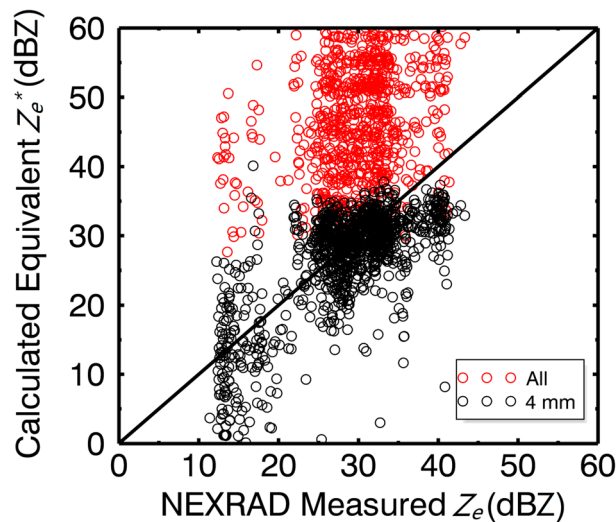


Figure 3. Comparisons between the calculated equivalent radar reflectivity factors Z_e^* using in situ measured full spectrum of raindrop size distributions (DSDs) (red circles) and the DSDs < 4 mm (black circles) with the collocated NEXRAD-measured radar reflectivity factors (Z_e) along the aircraft flight tracks (a total of 1126 five second averaged samples in this study).

to 49% at $2800 \mu\text{m}$ because the HVPS probe is capable of measuring larger raindrops than the 2DC probe (raindrops were reconstructed for $D > 1000 \mu\text{m}$) [Heymsfield and Parrish, 1978; Korolev, 2007]. One possible reason for the discrepancy is the difference in sample volume between the two probes. Further investigations were also carried out for bulk properties of total number concentration (N_t) and liquid water content (LWC). The averaged ratios of N_t and LWC (2DC over HVPS) are 1.41 and 1.24, respectively, showing general consistency between the two optical array probes. As a result, in this study we use the DSD spectrum ranges from $120 \mu\text{m}$ to $4000 \mu\text{m}$ through a combination of 2DC (120 to $900 \mu\text{m}$) and HVPS (900 to $4000 \mu\text{m}$) probe data. Both the 2DC and HVPS probes were well calibrated by the manufacturers before the field campaign, and performance checks and quality control procedures were carried out before and after each flight. To further control the quality of the data, 20% of the optical array probe (OAP) records were rejected due to either insufficient sampling or nonsimultaneous recordings between two OAPs.

2.2. Ground-Based Radar Observations

Based on the Next Generation Weather Radar (NEXRAD, S-band) network of Weather Surveillance Radar-1988 Doppler (WSR-88D) radars, the NOAA National Severe Storms Laboratory produces a national (CONUS) 3-D gridded radar mosaic coverage with 1 km horizontal resolution, 31 vertical levels (resolution varies from 200 m to 2000 m), and 5 min temporal resolution (<https://www.nssl.noaa.gov/projects/q2/nmq.php>). As a key component in the NMQ system, the NEXRAD Q2 precipitation product was generated to quantitatively estimate the surface rain rate by choosing an appropriate Z-R relationship [Zhang et al., 2011]. The high-resolution 3-D gridded radar mosaic was used to extract the large-volume cloud bulk properties (the equivalent reflectivity factor Z_e) collocated with the UND aircraft flight track, which served as an independent data source to evaluate the representation and calculations of in situ measurements.

Figure 3 illustrates the comparisons between the calculated equivalent radar reflectivity factor (Z_e^*) using the in situ measured DSDs (5 s averaged, a flight distance of ~ 500 m) and the collocated NEXRAD radar reflectivity observations (Z_e , sampled along the aircraft track). The black circles in Figure 3 represent the calculated results using the size spectral range mentioned in section 2.1 (120 to $4000 \mu\text{m}$), and the red circles were generated from the full spectrum. The radar equation is given by

$$Z_e^* (\text{mm}^6 \text{ m}^{-3}) = 10^{12} \int_{D_{\min}}^{D_{\max}} N(D) D^6 dD, \quad (1)$$

where D_{\min} ($120 \mu\text{m}$) and D_{\max} ($4000 \mu\text{m}$) are the integral limits, D is the diameter of the smallest circle that encloses the raindrop image [Heymsfield and Parrish, 1978; Field et al., 2006; Korolev, 2007], and $N(D)$ is number

to occur at the large size of the spectrum. Second, the cumulative probability in Figure 2b shows that the surface measured raindrop diameters greater than 4 mm only represent 1.3% of the entire distribution, which will not have a strong impact on the calculation of bulk properties. Finally, excluding the portion of $D > 4$ mm benefits the DSD fitting process by reducing the uncertainties from artifacts. This is also consistent with the results of Wang et al. [2015], where the maximum diameter of the ice crystal aggregates is 30 mm (equivalent to the maximum raindrop diameter of ~ 4 mm in Figure 2a).

For the overlapping spectral region (DSD = 900 – $2800 \mu\text{m}$) measured by both the 2DC and HVPS, the frequency of occurrence for particles recorded by each size bin was calculated. Their differences increase from 42% at $900 \mu\text{m}$

Table 1. Summary of Surface Rain Rate Measurements

	Location (Longitude, Latitude)	Precipitation Amount Detectability (mm)	DSD Observations	Temporal Resolution	Data Source
RD-80 2DVDs	−97.485, 36.605 (SGP CF)	0.0001	20 size bins 0.3 to 5.4 mm	1 min	https://www.arm.gov/instruments/disdrometer ftp://gpm.nsstc.nasa.gov/gpm_validation/mc3e/disdrometers_and_gauges/2dvd/data/
	−97.532, 36.624 (SN25)	0.00017 (0.01 mm h ^{−1})	41 size bins 0.1 to 10 mm	1 min	
	−97.480, 36.618 (SN35)				
	−97.479, 36.581 (SN36)				
	−97.481, 36.633 (SN37)				
Mesonet	−97.445, 36.578 (SN38)				https://www.arm.gov/instruments/okm
	−97.254, 36.754 (BLAC)	0.254	N/A	5 min	
	−97.694, 36.412 (BREC)				
	−97.286, 36.147 (CARL)				
	−97.213, 36.064 (MARE)				
	−97.607, 36.119 (MARS)				
	−97.746, 36.792 (MEDF)				
	−97.153, 36.356 (REDR)				
	−97.095, 36.121 (STIL)				

concentration of corresponding D (all parameters except Z_e^* are in cgs units, and the aircraft bin scheme is shown in Appendix A, which will also be used in rain rate derivation). Apparently, the black circles converge much closer to the collocated NEXRAD Z_e observations than the red circles, suggesting the existence of elongated artifacts recorded by the HVPS at $D > 4$ mm, and those artifacts could be easily removed using the designated size threshold $D \leq 4$ mm in this study.

Another important assumption used in calculating reflectivity factor is the constant axis ratio of 0.7, in which axis ratio is defined as vertical dimension over the horizontal dimension of the raindrops [Jameson and Beard, 1982]. As suggested by Chandrasekar *et al.* [1988], by eliminating the influence of the rotation angle of raindrops, the axis ratio can be equivalent to the aspect ratio (the ratio of maximum dimension of raindrops along and across the scan direction). In addition, with the assumption of an oblate shape, the aspect ratio of raindrops defined by Korolev and Isaac [2003] (i.e., D_w/D_{\max_d} , where D_{\max_d} is the maximum dimension of raindrops and D_w is the maximum dimension of raindrops in the direction perpendicular to D_{\max_d}) is equal to the well-accepted area ratio (the ratio of the projected area of raindrops to the area of a circumscribed circle) [McFarquhar and Heymsfield, 1996] according to the following derivation:

$$\text{Area ratio} = \frac{\text{Area of Ellipse}}{\text{Area of Maximum Circle}} = \frac{\frac{\pi}{4} D_{\max_d} D_w}{\frac{\pi}{4} D_{\max_d}^2} = \frac{D_w}{D_{\max_d}} = \text{Aspect Ratio}, \quad (2)$$

As a result, by assuming an oblate shape and disregarding the discrepancy in definitions of aspect ratio, the area ratio could serve as a good approximation of the axis ratio. In this study, the averaged area ratio (0.7) was used in calculation of Z_e^* for simplicity.

It is worthwhile to note that some outliers shown in Figure 3 may be attributed to the mismatch in sample volumes between aircraft in situ and radar observations as discussed in Mace *et al.* [2002] and Dong *et al.* [1998, 2002]. The sample volume of the radar is a few orders of magnitude larger than in situ probes, which makes the representativeness of in situ measurements greatly depend on the homogeneity of large-volume samples observed by radar [Ryzhkov *et al.*, 2005a, 2005b; Ryzhkov 2007]. In addition, a minor error could also be introduced by interpolating radar data from coarse to high temporal resolution.

The NOAA Earth System Research Laboratory Physical Sciences Division S-band precipitation profiler [Ecklund *et al.*, 1999] was deployed at the ARM SGP site during MC3E. This instrument measured the vertical structure of DCSs at 1 min temporal resolution and 62 m vertical resolution ranging from 200 m to 1600 m above the ground. With an adequate sensitivity in reflectivity factor (−14 dBZ at 10 km) and finer resolutions, the NOAA S-band radar reflectivity serves as the “ground truth” to evaluate the performance of NEXRAD mosaic data.

2.3. Surface Rain Rate Measurements

A brief summary of the instruments used for measuring precipitation characteristics and rainfall is listed in Table 1. In addition to precipitation properties including rain rate and radar reflectivity, the RD-80

disdrometer also provided the most continuous DSD measurements at high spectral and temporal resolutions along with routinely fitted DSD exponential parameters, at the ARM SGP site during MC3E. Taking advantage of the detailed DSD information, the intercomparisons of cloud-base reflectivity factors between the radar observations and the RD-80 reconstructions, as well as the NEXRAD-retrieved and RD-80-provided exponentially fitted parameters, were conducted for the ARM SGP site, which will be discussed in section 3. As for quality control of the surface measurements, both the spurious raindrops (e.g., likely caused by splash or insects) and sparse observations (fewer than 10 raindrops or rain rate less than $0.01 \text{ mm h}^{-1} \text{ min}^{-1}$) were eliminated in this study [Tokay *et al.*, 2001]. Note that the data provided by the RD-80 were not used for DSD parameterization but for validating retrieved precipitation. In addition, the correction for dead time (underestimation for the number concentration at small drops in heavy precipitation events [Waldvogel, 1974; Sheppard and Joe, 1994]) was not performed during this study. The 2DVDs had a considerable amount of time intervals with missing data (e.g., more than 3 h of void values for the SN35 site on 20 May 2011 from 10:40 to 14:56 UTC). Due to intrinsic instrumental limitations, the unheated tipping-bucket rain gauges used in the Oklahoma Mesonet network have a coarse detectability of 0.254 mm (one tip) with a temporal resolution of 5 min.

In order to temporally match the observations from different instruments, i.e., NEXRAD (5 min), NOAA S-band radar (1 min), RD-80 disdrometer (1 min), 2DVDs disdrometers (1 min), and the Mesonet tipping-bucket (5 min), the temporal resolution was set to 5 min for the surface rain rate measurements in this study. That is, the 1 min rain rate measurements from the RD-80 and 2DVDs disdrometers were resampled with each 5 min interval to match the 5 min Mesonet tipping-bucket measurements. To avoid spatial mismatches between in situ measurements, ground-based radar observations, and surface rain rate measurements, the study domain was confined to a $1^\circ \times 1^\circ$ grid box centered on the ARM SGP site (Figure 1a), where the disdrometers and Mesonet tipping buckets, as well as aircraft flights, were all located (Figure 1b).

3. New DSD Parameterization Scheme and Its Application for Precipitation Estimation

In this section, a full spectrum of rain DSDs was constructed through a combination of 2DC (120 to $900 \mu\text{m}$) and HVPS (900 to $4000 \mu\text{m}$) measurements. A total of 1126 five second in situ measured DSDs were fitted with exponential size distributions and then parameterized as a function of the radar reflectivity, according to its theoretical definition (equation (1)). In order to assess the new parameterization scheme incorporating the dependencies between DSD parameters, the rain rates were calculated using the retrieved DSDs from NEXRAD reflectivity at cloud base and then compared with the surface rain rate measurements. Lastly, the NEXRAD Q2 precipitation estimate is compared with the calculated and measured surface rain rates.

3.1. Fitting to the In Situ Measured DSDs

The Exponential function has been commonly used in representing DSD for its simplicity in connecting DSD-based bulk properties for different moments (e.g., sixth-moment radar reflectivity and roughly third-moment rain rate [Marshall and Palmer, 1948]). Since the publication of the classic paper [Ulbrich, 1983], a three-parameter Gamma function has drawn more attention. Following the same fitting techniques used in ice cloud properties of DCSs [Press *et al.*, 1992; McFarquhar *et al.*, 2007; Wang *et al.*, 2015], a total of 1126 five second DSDs have been used to fit to the gamma function as follows (in cgs units):

$$N(D) = N_0 D^\mu e^{-\lambda D}. \quad (3)$$

In (3), N_0 is the intercept ($\text{cm}^{-(4+\mu)}$), μ is the shape (dimensionless), λ is the slope (cm^{-1}), D is the raindrop diameter (cm), and $N(D)$ (cm^{-4}) is the corresponding number concentration at each bin [Heymsfield *et al.*, 2010]. Besides the Gamma function, a two-parameter Exponential function (where $\mu = 0$) was also performed to facilitate precipitation estimation from radar reflectivity, because the operationally gridded polarimetric radar observations were not available during MC3E.

Figure 4 shows a series of typical Gamma and Exponential fits to the averaged DSDs with collocated NEXRAD Z_e , ranging from 30 to 26 dBZ. At each individual time, the Gamma fitted results (red solid lines) demonstrate better agreement with the observed DSDs (blue bars), especially for drop sizes greater than 2 mm. However, for certain cases like Figure 4b, no significant differences in the overall shape, as well as the values of N_0 and λ

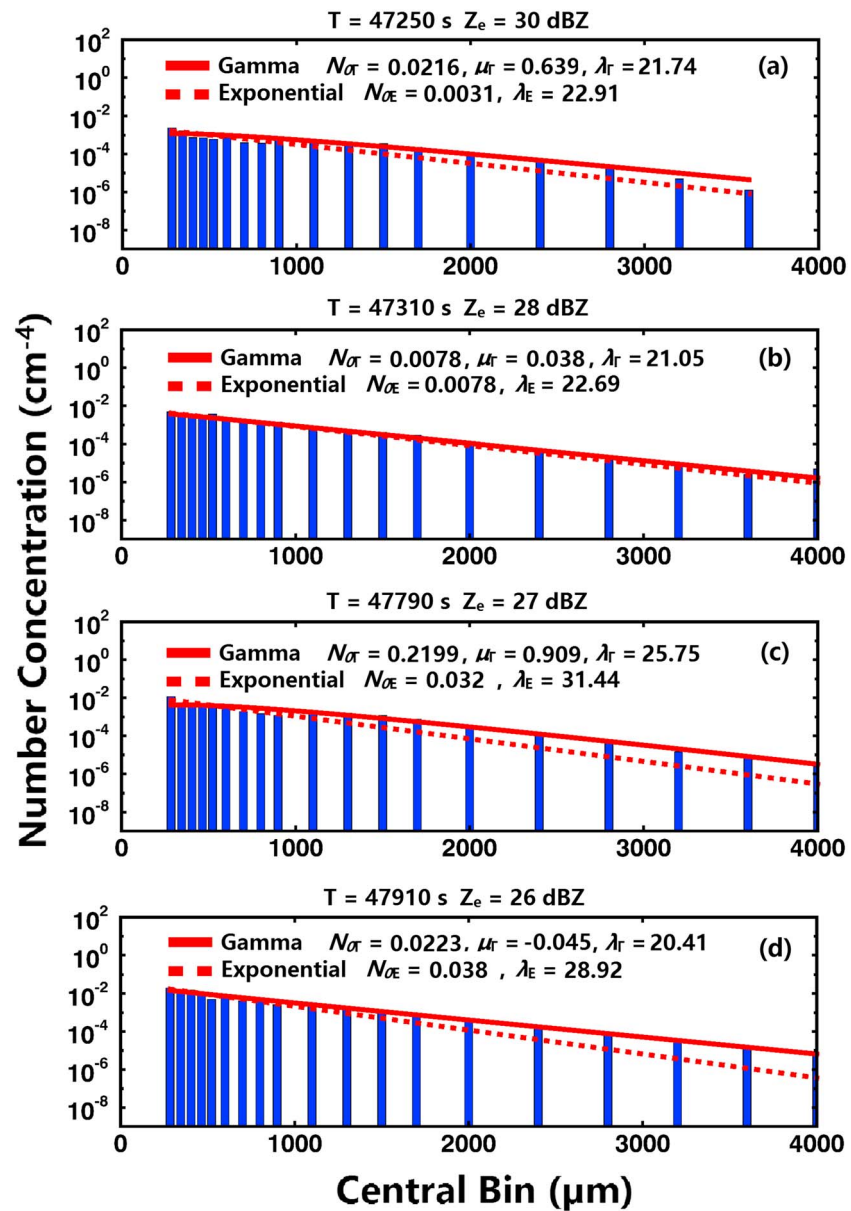


Figure 4. Variation of the fitted parameters of Gamma function ($N_{0\Gamma}$, μ_{Γ} , and λ_{Γ} in red solid lines) and Exponential function (N_{0E} and λ_E in red dashed lines) compared to the observed original DSDs (blue bars) with respect to time T (UTC) and NEXRAD radar reflectivity Z_e . (a) $T_1 = 47,250$ s (~ 13.125 UTC), $Z_e = 30$ dBZ. (b) $T_2 = 47,310$ s, $Z_e = 28$ dBZ. (c) $T_3 = 47,790$ s, $Z_e = 27$ dBZ. (d) $T_4 = 47,910$ s, $Z_e = 26$ dBZ, a few instances during the 20 May 2011 case.

parameters, were found between Gamma and Exponential fits, indicating that the Exponential function can capture most of the DSD shape information except for some of the large drops.

For Gamma parameters, Zhang *et al.* [2001] and Brandes *et al.* [2004] concluded that shape parameter (μ_{Γ}) is strongly related to the slope parameter (λ_{Γ}). Refined by Cao *et al.* [2008] and Cao and Zhang [2009] using surface 2DVD observations in Oklahoma, an applicable shape-slope (μ_{Γ} - λ_{Γ}) relationship was generated as $\mu_{\Gamma} = -0.0201 \lambda_{\Gamma}^2 + 0.902 \lambda_{\Gamma} - 1.718$ (black dashed line in Figure 5a). Similarly, a second-order polynomial regression was fitted from the aircraft data (black solid line in Figure 5a). Figure 5a clearly demonstrates that the two trends from Cao *et al.* [2008] and Cao and Zhang [2009] and this study are nearly the same for the λ_{Γ} values ranging from 0 mm⁻¹ to 6 mm⁻¹ (note that the cgs units were not used in μ_{Γ} - λ_{Γ} relationship for consistency with previous studies). For $\lambda_{\Gamma} > 6$ mm⁻¹, these two trends start to deviate and their differences increase with increasing λ_{Γ} . These differences can either be attributed to the 2DVDs's undersampling issue

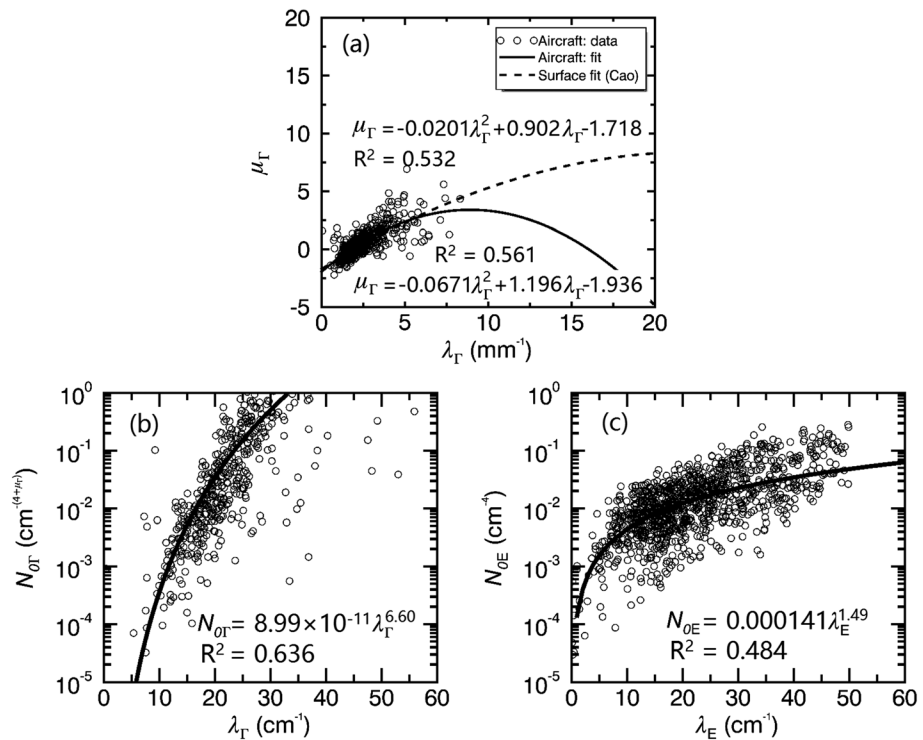


Figure 5. (a) Gamma fitted DSD shape parameter μ_Γ as a function of slope parameter λ_Γ . (b) Gamma fitted DSD intercept parameter $N_{0\Gamma}$ as a function of slope parameter λ_Γ . (c) Exponentially fitted DSD intercept parameter N_{0E} as a function of slope parameter λ_E .

for drop sizes greater than 3 mm as discussed in *Cao et al.* [2008] or that sorting and averaging methods based on the two parameters were not employed in aircraft data processing due to limited number of samples. Nonetheless, by applying the equation from *Cao et al.* [2008] to aircraft data, the coefficient of determination (R^2) is 0.532, which is comparable to the new fitting result ($R^2 = 0.561$). The similar μ_Γ - λ_Γ relationships generated from aircraft in situ data aloft in this study and surface disdrometer measurements in *Cao et al.* [2008] have demonstrated that two independent platforms at different elevations can capture similar DSD attributes.

In addition to the shape-slope relationship, Figure 5b exhibits the intercept-slope ($N_{0\Gamma}$ - λ_Γ) relationship for the Gamma fits. Similar to the finding of *Ulbrich* [1983], $N_{0\Gamma}$ values fluctuated by several orders of magnitude (in this case from 10^{-5} to $10^6 \text{ cm}^{-(4+\mu_\Gamma)}$, not completely shown in Figure 5b), which limits the utility of the $N_{0\Gamma}$ - λ_Γ relationship in studies of cloud and precipitation microphysics. However, for the parameters from the Exponential fits (Figure 5c), most of the N_{0E} values fall within a range from 10^{-3} to 10^{-1} cm^{-1} , indicating that setting $\mu_\Gamma = 0$ is the simplest assumption from the perspective of constraining the variation in the intercept parameter [*Tian et al.*, 2007; *Liao et al.*, 2014; *Williams et al.*, 2014]. To verify the validity of $\mu_\Gamma = 0$, the probability density function (PDF) of μ_Γ values generated from aircraft in situ data is shown in Figure 6, where it basically follows the Gaussian distribution with a mean value of 0.58 and a standard deviation of 1.15. This result has demonstrated that the approximation of the Gamma function using an Exponential function with the assumption of $\mu_\Gamma = 0$ is valid and reasonable. Note that the μ_Γ - λ_Γ relationship generated in Figure 5a cannot be applied to the λ_Γ values greater than 6 mm^{-1} , and the N_{0E} - λ_E relationship shown in Figure 5c cannot be applied to the λ_E values greater than 60 cm^{-1} .

Figures 5 and 6 exhibit additional information about the ranges of μ_Γ and λ_Γ values from this study and from *Cao et al.* [2008]. The λ_Γ values range from 0 mm^{-1} to 20 mm^{-1} , and the μ_Γ values are from -3 to 15 in *Cao et al.* [2008], whereas both the λ_Γ and μ_Γ values in this study have limited ranges (with 95% tolerance interval of $[-1.72, 2.88]$ for μ_Γ). The different ranges from these two studies using two independent platforms at different elevations may represent the real nature of the DSD shape information in clouds and at the surface. These aircraft in situ data can directly provide statistical information of the DSD shape parameters during MC3E for the study of cloud-to-precipitation processes (e.g., breakup and collision), where the initial DSDs aloft in most of the

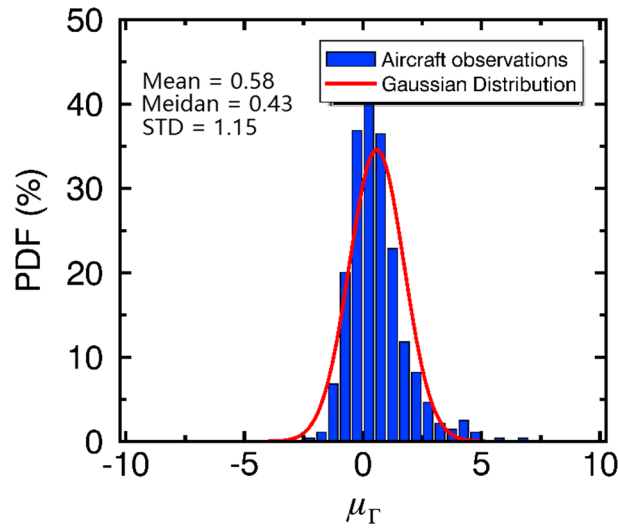


Figure 6. Probability density function of Gamma fitted shape parameter (μ_Γ) from aircraft data (blue bars) and Gaussian with mean value of 0.58 and standard deviation of 1.15 (red line).

previous studies were either fixed or simplified [McFarquhar, 2004a, 2004b]. In summary, the similar μ_Γ - λ_Γ relationships but different μ_Γ and λ_Γ value ranges generated from two independent platforms at different elevations have demonstrated that it is helpful to study DSD changes from clouds to precipitation, using a combination of aircraft in situ measurements in clouds and disdrometer measurements at the surface.

3.2. Semiempirical Relationships Between Fitted DSD Parameters and Z_e

Compared to surface disdrometer measurements which are several hundreds of meters below the radar echo base, aircraft in situ measurements and radar observations can be easily collocated both spatially and temporally. Using air-

craft in situ measurements does reduce the problem of the variation of the DSD from cloud base to the surface. More importantly, aircraft in situ probes can provide much larger sample volume (400 L s^{-1} for HVPS at the flight speed of 100 m s^{-1}) and better temporal resolution compared to surface disdrometers (5 L s^{-1} for RD-80 with 50 cm^2 sample area and a 1 m s^{-1} assumption of vertical air speed). For application of the fitted DSD parameters to precipitation estimation using NEXRAD Z_e , the N_{0E} - λ_E relationship is generated and presented in Figure 5c from a total of 1126 five second samples. The new power-law relationship is presented as

$$N_{0E} = 0.000141 \lambda_E^{1.49}, \quad (4)$$

with coefficient of determination ($R^2 = 0.48$). Note that the N_{0E} - λ_E relationship derived from the RD-80 disdrometer measurements may introduce larger uncertainties than that derived from aircraft in situ measurements, due to the limited sample volume. This is another major reason that the N_{0E} - λ_E relationship was established here using the aircraft in situ measurements rather than from RD-80 disdrometer measurements. Substituting (3) into (1) (with $\mu = 0$ and integral limits from 0 to ∞), Z_e^* becomes

$$Z_e^* (\text{mm}^6 \text{ m}^{-3}) = 10^{12} \int_0^\infty N_{0E} e^{-\lambda_E D} D^6 dD. \quad (5)$$

Following the Euler integral of the second kind [Jeffrey and Dai, 2008] ($\Gamma(t) = \int_0^\infty x^{t-1} e^{-x} dx$), Z_e^* can be expressed in the product of N_0 and λ :

$$Z_e^* (\text{mm}^6 \text{ m}^{-3}) = 10^{12} N_{0E} \lambda_E^{-7} \Gamma(7). \quad (6)$$

Finally, by substitution of (4) into (6), the slope parameter λ can be directly calculated from radar reflectivity Z_e^* :

$$\lambda_E = \left(\frac{0.10152 \times 10^{12}}{Z_e^* (\text{mm}^6 \text{ m}^{-3})} \right)^{\frac{1}{5.5}}. \quad (7)$$

The major concern of this derivation is the substitution of the complete Gamma function (integral from 0 to ∞) with an incomplete Gamma function (integral from D_{\min} to D_{\max}), whose differences were thoroughly discussed by McFarquhar et al. [2015]. For the x th moment (M_x) of a DSD,

$$M_x = \int_{D_{\min}}^{D_{\max}} N_0 D^x e^{-\lambda D} D^x dD = \frac{N_0}{\lambda^{x+\mu+1}} [\Gamma(x+\mu+1, \lambda D_{\max}) - \Gamma(x+\mu+1, \lambda D_{\min})], \quad (8)$$

and

$$\Gamma(u, v) = \int_0^v x^{u-1} e^{-x} dx. \quad (9)$$

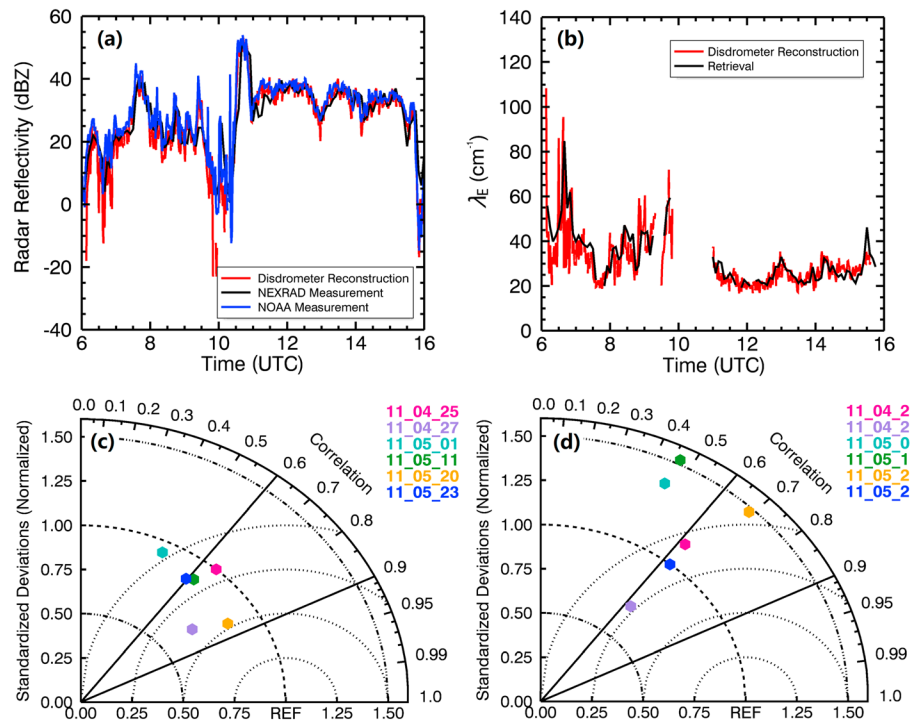


Figure 7. (a) Time series comparison among disdrometer reconstructed, NEXRAD measured, and NOAA S-band radar reflectivity factors at cloud base during 20 May 2011. (b) Comparison between disdrometer reconstructed exponential slope parameter λ_E and retrieved one from this study. (c) Taylor diagram of radar reflectivity factors at cloud base for all selected six cases. (d) The same as Figure 7c but in term of slope parameter λ_E .

In this study, we evaluated the influence of partial integrations (0 to D_{\min} and D_{\max} to ∞) in Z_e^* calculation compared to the Z_e^* values integrated from D_{\min} to D_{\max} , which we considered as the ground truth. The corresponding Z_e^* uncertainties are 0% for the integral portion from 0 to D_{\min} and 7% for the portion from D_{\max} to ∞ .

3.3. Application of Newly Parameterized DSDs for Precipitation Estimates and Assessment

Based on equations (4) and (7), the DSD variables can be parameterized as a function of radar reflectivity according to its theoretical definition. Therefore, the rain rate can be retrieved from the DSD parameters and NEXRAD cloud-base observed Z_e values. To evaluate the NEXRAD cloud-base reflectivity measurements within the SR regions of DCSSs, a performance check was conducted using collocated NOAA S-band radar observations at the NEXRAD cloud bases, as well as calculated Z_e^* values from the RD-80 disdrometer at the ARM SGP site. As shown in Figure 7a, there is an excellent agreement in cloud-base radar reflectivity between NEXRAD and NOAA S-band for the 20 May 2011 case, with averages of 27.0 and 28.7 dBZ during a 10 h period. Another interesting result is that the average of the calculated Z_e^* values using surface RD-80 disdrometer measurements is 26.7 dBZ, which is nearly the same as the NEXRAD cloud-base radar observations. The mean differences of 0.3 dBZ and 1.7 dBZ indicate that the NEXRAD cloud-base reflectivity measurements are reliable for precipitation retrieval. As for all cases, a Taylor diagram (polar coordinate system) was generated in Figure 7c, where the correlation coefficients (shown as the rotation angle from the vertical axis) between NEXRAD and NOAA S-band reflectivity measurements range from 0.44 to 0.85, and the normalized standard deviations (standard deviation of NEXRAD divided by standard deviation of NOAA S-band, shown as the distance from coordinate origin) range from 0.68 to 1.00.

Figure 7b shows another comparison in slope λ_E between calculated values from equation (7) using NEXRAD cloud-base Z_e values and the ones provided by RD-80 measurements, for the SR regions of the 20 May 2011 case. There are no λ values between 1000 and 1100 UTC because the convective region passed directly over the ARM SGP site. Notice that prior to 1000 UTC, there are relatively large variations in both Z_e and λ_E values, and their

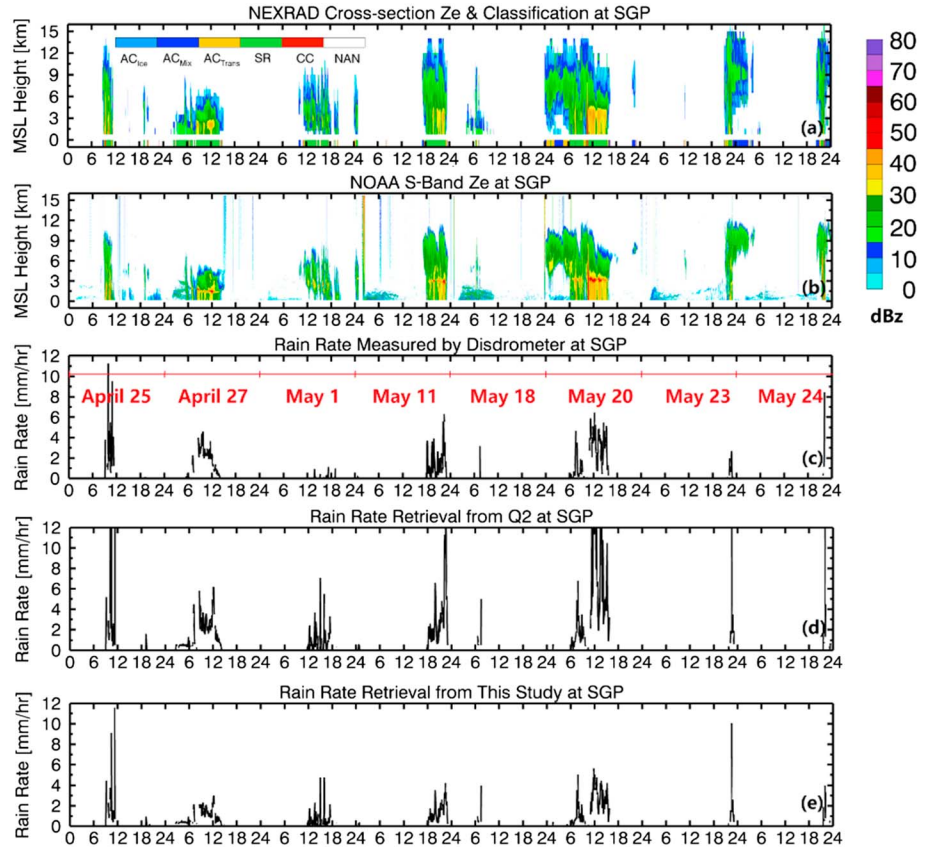


Figure 8. Time series of (a) NEXRAD cross-sectional radar reflectivity factors and CSA classification (at bottom), (b) NOAA S-band radar reflectivity factors, and rain rates for SR regions from (c) the RD-80 surface disdrometer measurement, (d) Q2 product, and (e) retrieval generated by this study over the ARM SGP site.

differences are also large, while after 1100 UTC (except 1530–1600 UTC), both Z_e and λ_E values are nearly invariant and their differences are almost indistinguishable. These discrepancies could be attributed to the convection types before and after the overpass of the convective system. Prior to the squall line passage, there was isolated convection over the SGP region, whereas afterward, there was widespread stratiform precipitation.

Similar to Figure 7c, Figure 7d shows the correlation coefficients and normalized standard deviations of λ_E values from selected cases with most correlation coefficients ranging from 0.6 to 0.7, and normalized standard deviations from 0.75 to 1.5, except for the 1 and 11 May 2011 cases. The large discrepancies for these two cases may result from the error propagated from the input (Z_e), the uncertainty from the RD-80 DSD measurements, and the Exponential fitting scheme used to calculate slope parameters. It is necessary to note that the statistical information was generated from a limited number of classified SR cloud samples directly over the ARM SGP site. For example, the 18 and 24 May 2011 cases were not shown in Figure 7, because there were less than ten 5 min SR samples. However, more than 80% of the total SR samples (27 April and 20 May 2011) showed good agreement with other independent observations (correlation coefficients greater than 0.8 for Z_e and greater than 0.6 for λ_E).

Finally, the rain rate can be calculated as follows:

$$RR(\text{mm/h}) = 3.6 \times 10^6 \int_{D_{\min}}^{D_{\max}} N_{0E} e^{-\lambda_E D} \frac{\pi}{6} D^3 V(D) dD. \quad (10)$$

Substituting equations (4) and (7) into (10), it becomes

$$RR(\text{mm/h}) = 3.6 \times 10^6 \int_{D_{\min}}^{D_{\max}} 0.000141 \left(\frac{0.10152 \times 10^{12}}{Z_e (\text{mm}^6 \text{ m}^{-3})} \right)^{\frac{1.49}{5.5}} e^{-\left(\frac{0.10152 \times 10^{12}}{Z_e (\text{mm}^6 \text{ m}^{-3})} \right)^{\frac{1}{5.5}} D} \frac{\pi}{6} D^3 V(D) dD, \quad (11)$$

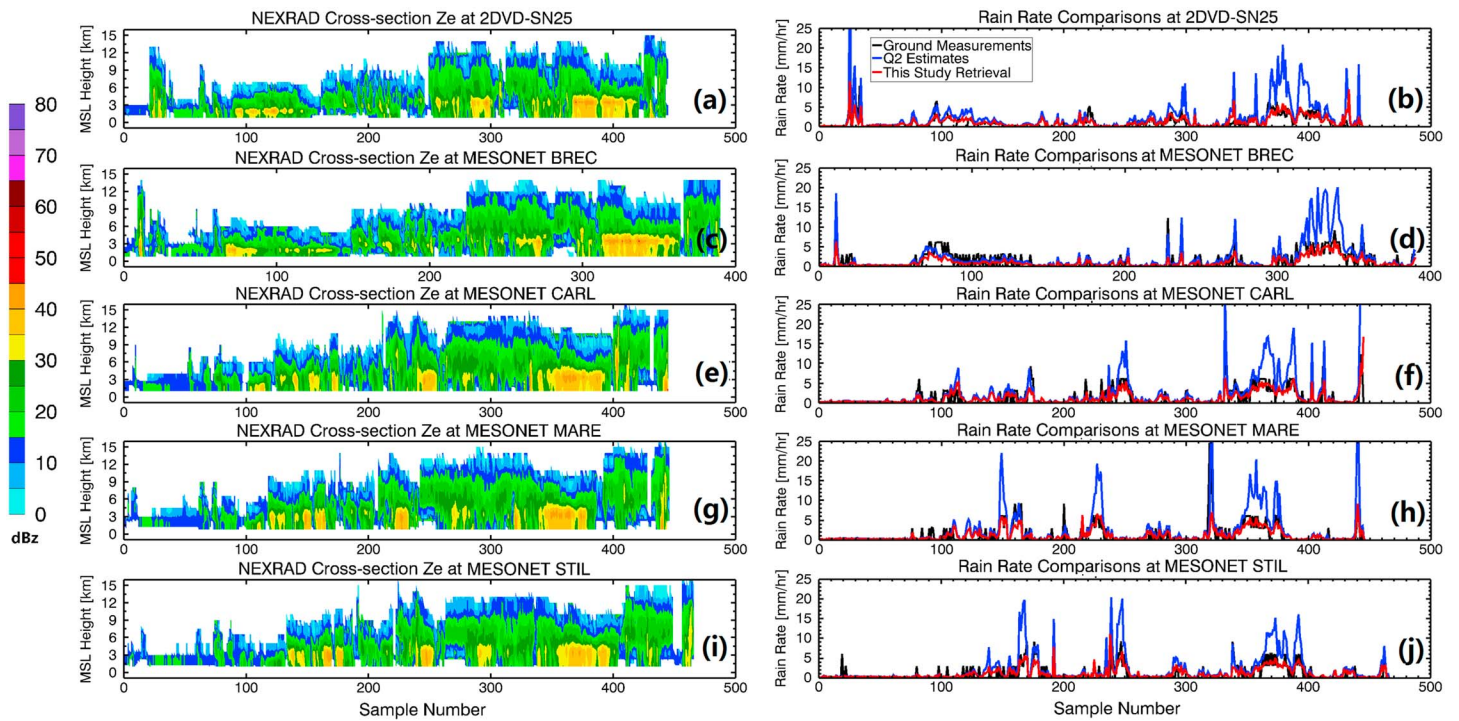


Figure 9. (a, c, e, g, and i) Same as Figure 7a but only the SR samples identified by UND CSA algorithm were extracted from the eight selected cases in this study. (b, d, f, h, and j) Comparisons among measured surface rain rates (black lines), Q2 products (blue lines), and retrievals from this study (red lines) at 2DVD-SN25, BREC, CARL, MARE, and STIL stations.

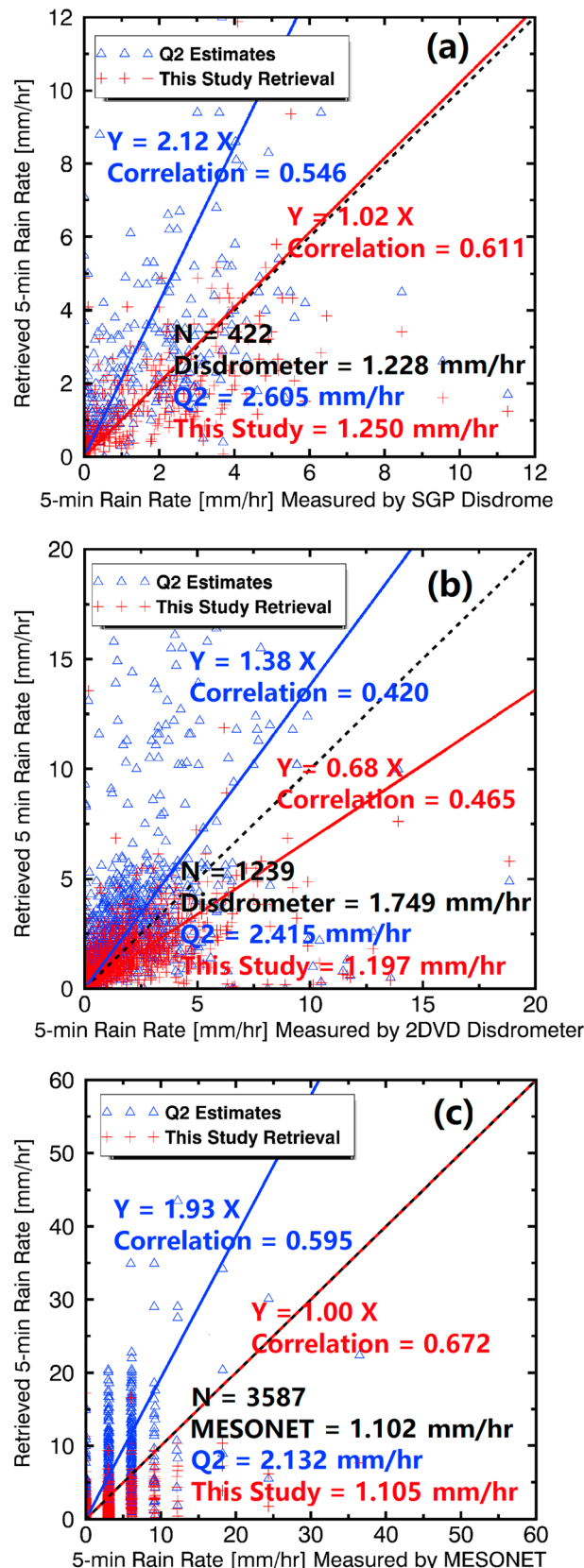
where $V(D)$ (in unit of m s^{-1} , and D is in unit of m) is the terminal velocity calculated following the method of Gunn and Kinzer [1949],

$$V = \sqrt{\frac{4}{3} \frac{Dg(\rho_{\text{water}} - \rho_{\text{air}})}{C\rho_{\text{air}}}}, \quad (12)$$

where the sea level condition is assumed with $g = 9.8 \text{ m s}^{-2}$, $\rho_{\text{water}} = 1000 \text{ kg m}^{-3}$, $\rho_{\text{air}} = 1.225 \text{ kg m}^{-3}$, and $C = 0.5$, at the standard atmospheric pressure of 1013.25 hPa. All units in equations (10) and (11) are in cgs except for special notations.

Figure 8 shows the time series of NEXRAD and NOAA S-band radar reflectivity factors, and three rain rates for the SR regions measured by the surface RD-80 disdrometer, extracted from the Q2 product and retrieved from this study for the ARM SGP site. It is necessary to note that the UND Convective-Stratiform-Anvil (CSA) algorithm was performed for cloud classification and only the rain rates for SR regions were extracted and compared in the following discussion. Compared to the NOAA S-band radar observations, NEXRAD suffers severe artifact issues above 10 km, which is consistent with the conclusion from Homeyer [2014] and Homeyer and Kumjian [2015]. Those artifacts could result from the limited vertical sampling issue of the NEXRAD radars. However, for the near-surface observations, as discussed above and shown in Figures 8a and 8b, NEXRAD cloud-base reflectivity measurements are compatible with NOAA S-band measurements in the SR regions of DCSs. For SR rain rate comparisons, the averaged Q2 estimation (Figure 8d) is much larger (2.605 mm h^{-1}) than the corresponding surface disdrometer measurement (1.228 mm h^{-1} , Figure 8c, serve as the best estimate in this study). On the contrary, the averaged SR rain rate retrieved from this study (1.218 mm h^{-1}) is almost identical to the best estimate as illustrated in Figure 8, as well as in Figures 9 and 10. These comparisons also reveal that the Q2 SR precipitation estimation based on Marshall-Palmer Z-R relationship [Marshall and Palmer, 1948], where a constant DSD intercept parameter (N_{0E}) was assumed, needs to be improved for heavy precipitation cases.

In addition to the SR rain rate comparisons over the ARM SGP site, the results from five more surface sites are extracted and presented. Figure 9 shows NEXRAD reflectivity (Figures 9a, 9c, 9e, 9g, and 9i) and rain



rate comparisons (Figures 9b, 9d, 9f, 9h, and 9j) among Q2 product, surface measurement, and retrieval from this study at the sites of 2DVD-SN25 (Figures 9a and 9b), BREC (Figures 9c and 9d), CARL (Figures 9e and 9f), MARE (Figures 9g and 9h), and STIL (Figures 9i and 9j). Similar conclusions can be drawn from these comparisons; that is, over these five additional surface sites the Q2 product severely overestimates the rain rates, especially for heavy rain cases, while the retrieval from this study is nearly identical to the surface rain rate measurement.

To further assess the Q2 product and retrieval from this study, the surface rain rate measurements from all disdrometers and Mesonet stations listed in Figure 1a are used as the best estimate. As shown in Figure 10, the averaged ratios of Q2 product to the best estimate are 2.12 at the ARM SGP site (Figure 10a), 1.38 at five 2DVD sites (Figure 10b), and 1.93 at eight Mesonet stations (Figure 10c) with corresponding correlation coefficients of 0.546, 0.42, and 0.595, respectively. The averaged ratios of the retrieval from this study to the best estimate are 1.02, 0.68, and 1.00 for different sites, with ~ 0.05 higher correlation coefficients. The comparison over five 2DVD sites is not as good as expected, primarily due to the missing data issue as discussed in section 2.3.

Based on the available disdrometers and rain gauges in Figure 1a, the spatial distributions of daily accumulated SR precipitation amount are presented over a $1^\circ \times 1^\circ$ domain in Figure 11. Figures 11c, 11h, 11m, and 11r exhibit the daily accumulated SR precipitation amount extrapolated from 14 scattered surface measurements on 1, 11, 20, and 24 May 2011. Similarly, Figures 11b, 11g, 11l, and 11q were generated by extrapolation for the locations of 14 surface sites using

Figure 10. Statistical comparisons of 5-min rain rates among disdrometer and Mesonet measurements, Q2 product, and retrieval from this study at (a) the ARM SGP site, (b) 2DVD stations, and (c) Mesonet stations for SR regions.

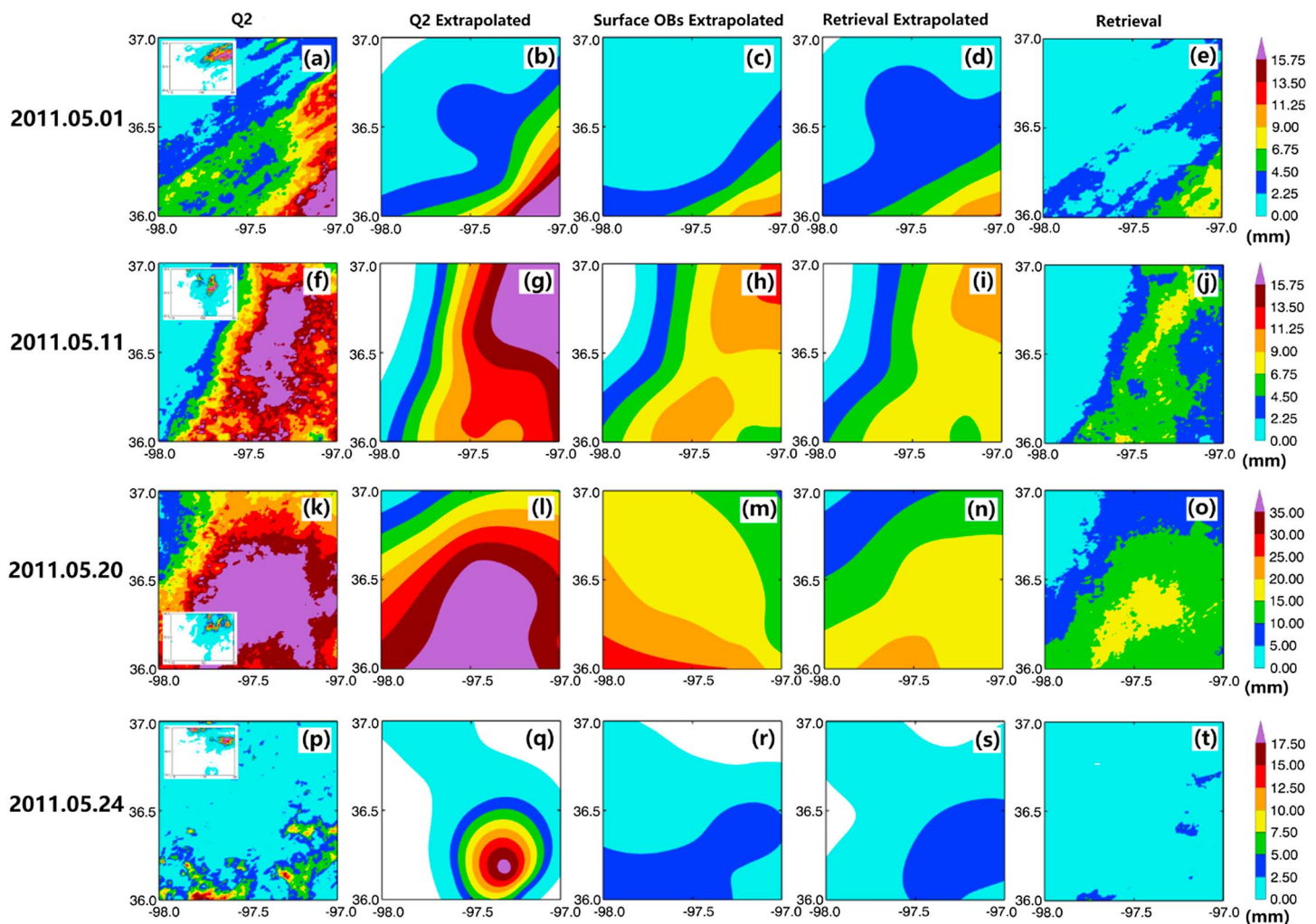


Figure 11. Spatial distributions of daily accumulated SR precipitation amount from original (a, f, k, and p) Q2 precipitation estimation and (e, j, o, and t) retrievals from this study, as well as the extrapolated results at the locations of 14 available disdrometer and Mesonet stations using the data extracted from (c, h, m, and r) direct measurements, (b, g, l, and q) Q2 estimation, and (d, i, n, and s) this study's retrievals, over a domain of $1^\circ \times 1^\circ$ centered on the ARM SGP site on 1 May, 11 May, 20 May, and 24 May.

the data extracted from original Q2 estimation (Figures 11b, 11g, 11l, and 11q), and Figures 11d, 11i, 11n, and 11s represent the extrapolated results using the data from the original retrieval in this study (Figure 11e, 11j, 11o, and 11t). Apparently, the extrapolated Q2 results (Figures 11b, 11g, 11l, and 11q) are much higher than the surface best estimate (Figures 11c, 11h, 11m, and 11r) across the entire study domain, especially over the heavy precipitation regions, which is consistent with the findings in Figures 8–10. On the other hand, similar spatial precipitation patterns between the surface best estimate and the retrieval from this study (Figures 11d, 11i, 11n, and 11s) are found from four cases. Note that by comparing the extrapolated results with their original high-resolution ones, the spatial extrapolation is not always optimal in capturing all detailed features because of the limited number of surface sites. The purpose of comparisons in Figure 11 is to demonstrate that the overestimation issue in Q2 product can become more problematic spatially than site by site, which can significantly impact the local hydrological cycle by the large positive bias in areal rainfall. However, the retrieval from this study exhibits good agreement with direct measurements in spatial precipitation patterns.

3.4. Evaluation of Marshall-Palmer Z-R Relationships Used in Q2 Precipitation Estimates

The Q2 SR precipitation estimates are based on the Marshall-Palmer Z-R relationship [Marshall and Palmer, 1948], while this study uses newly generated DSD parameterization scheme to retrieve SR precipitation. Therefore, it is necessary to have an in-depth investigation of the similarities and differences between the two methods. As suggested by Khain *et al.* [2015] and Patade *et al.* [2015], using fixed DSD parameters is

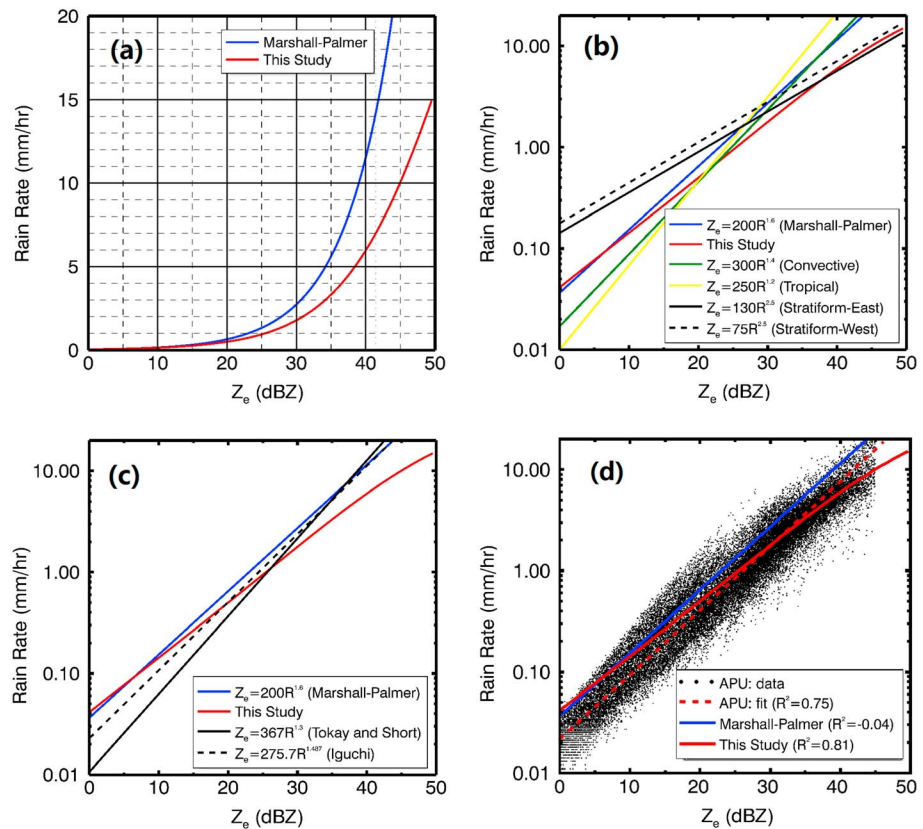


Figure 12. (a) Comparison in Z - R curves between Marshall-Palmer (blue line) and this study (red line). (b) Similar to 12a but in logarithmic scale and five operational schemes were included to have Q2 precipitation estimate: convective (green), tropical (yellow), stratiform east (black), and stratiform west (dash black). (c) Comparisons among Marshall-Palmer (blue line), this study (red line), Tokay and Short [1996] SR scheme, and Iguchi et al. [2000] SR scheme. (d) All the valid Z_e and corresponding rain rate records for SR regions from 17 Automatic Parsivel Unit (APU) sites during the entire MC3E campaign (22 April 2011 to 6 June 2011, black dots), as well as the Z - R relationships from Marshall-Palmer (blue line), this study (red solid line), and the direct regression line of APU observations (red dash line).

not an optimal approximation and may lead to a substantial misrepresentation of the cloud microphysics. In Marshall and Palmer [1948], the assumption of constant N_0 (0.08 cm^{-4}) was applied to construct the power-law Z - R relationship, which ignored the natural relationship between N_{0E} and λ_E . On the other hand, the fitted $N_{0E}\lambda_E$ relationship (equation (4)) was used to develop a new Z - R relationship over the SR regions in this study. Figure 12a compares the Z - R relationships from Marshall-Palmer ($Z_e (\text{mm}^6 \text{ m}^{-3}) = 200R^{1.6}$, R in mm h^{-1}) and this study (equation (11)), where the differences between these two Z - R relationships are indistinguishable for $Z_e < 20 \text{ dBZ}$, but the differences start to increase with increased Z_e values for $Z_e > 20 \text{ dBZ}$. This helps to explain the severe overestimation in Q2 precipitation estimates shown in Figures 8–11.

Figure 12a probes the following two questions: (a) is the Q2 classification consistent with the UND Convective-Stratiform-Anvil (CSA) classification for SR regions of DCSs and (b) what if other Z - R relationships were used in precipitation estimation for those regions? To answer these two questions, Figure 12b presents four more operational Z - R relationships [Nelson et al., 2010] in addition to Marshall-Palmer for the SR precipitation estimation (Figure 12a). They are convective ($Z_e = 300R^{1.4}$), tropical ($Z_e = 250R^{1.2}$), stratiform east ($Z_e = 130R^{2.5}$), and stratiform west ($Z_e = 75R^{2.5}$). Figure 12b clearly demonstrates that the retrieval from this study agrees well with the Q2 rain rate estimation using Marshall-Palmer Z - R relationship for $Z_e < 20 \text{ dBZ}$ and outperforms other Z - R relationships. For example, with a given radar reflectivity of 15 dBZ , the rain rate retrieved from this study is 0.273 mm h^{-1} , which is close to the value of 0.316 mm h^{-1} using Marshall-Palmer Z - R relationship. However, severe underestimation can be found using the Z - R relationships for convective (0.200 mm h^{-1}) and tropical (0.179 mm h^{-1}), as well as an overestimation for stratiform east (0.568 mm h^{-1}) and stratiform west (0.708 mm h^{-1}). This comparison has confirmed that both Q2 and UND CSA algorithms

have correctly identified the SR regions of DCSs in this study; otherwise, the differences between Q2 and this study would be much larger than the current ones.

Unlike all other power-law Z - R relationships shown as straight lines in Figure 12b, the one developed in this study (red line) deviates more from the straight line pattern as Z_e increases beyond 20 dBZ. Figure 12c shows two other power-law SR Z - R relationships developed from Darwin, Australia [Tokay and Short, 1996], and TRMM precipitation [Iguchi et al., 2000], along with the Z - R relationships from Marshall-Palmer and this study. This comparison illustrates the “seesaw” patterns found using different samples based on power laws, and the choice of intercept and linear slope may be, to a great extent, influenced by the distribution of rain rate intensity sampled in their experiments. Figures 12b and 12c clearly demonstrate that linear Z - R relationships on logarithmic axes cannot accurately represent the actual nonlinear relationship found in this study, due to the intrinsic nature of the power-law relationship, whereby the downward curvature becomes increasingly prominent as Z_e increases above 20 dBZ.

To further test the newly developed Z - R relationship developed in this study, the surface rain rate measurements and corresponding reflectivity measurements for SR regions from a total of 17 APU (Automatic Parsivel Unit) sites during the entire MC3E (from 22 April to 6 June 2011) experiment were collected and processed as an independent data set to evaluate the different Z - R relationships. As demonstrated in Figure 12d, the rain rates calculated from our Z - R relationship (red solid line) have the best agreement with surface measurements and outperform those from power-law fits (red dash line) and the Marshall-Palmer relationship (blue solid line). More importantly, the APU data samples in Figure 12d show a nonlinear trend on a logarithmic scale, and the absolute slope difference relative to linear regression line (red dash line) seems to increase from 0 dBZ to 20 dBZ, and decrease from 20 dBZ to 45 dBZ, forming a downward curve. Coincidentally, the Z - R relationship from this study (red solid line) can capture the feature of downward curvature starting from 20 dBZ, while the other two straight lines demonstrate overestimation to different extents. For the portion from 0 dBZ to 20 dBZ, the rain rates estimated from Marshall-Palmer and new relationship are nearly the same, but both are overestimated. As shown in Figure 12d, the rain rates estimated from 0 dBZ to 20 dBZ are less than 0.5 mm h^{-1} , which falls into the uncertainties of detectability and has insignificant contribution to overall DCS precipitation. Figure 12d also illustrates that coefficients of determination (R^2) are -0.04 , 0.81 , and 0.75 , respectively, for the Z - R relationships from Marshall-Palmer, this study, and direct regression to the APU data for a typical SR reflectivity range from 0 dBZ to 45 dBZ. Based on the comparisons with other Z - R relationships and independent APU data, we can conclude that the newly developed Z - R relationship (equation (11)) in this study exhibits the best representation of APU data in both overall Z - R distribution's shape and quantitative analysis.

4. Summary and Conclusions

In this study, eight DCS cases sampled by the University of North Dakota Citation II research aircraft during MC3E were selected to investigate the liquid-phase ($T > 3^\circ\text{C}$) cloud and precipitation microphysical properties within DCSs. The in situ measurements were carefully processed and examined, and semiempirical relationships between DSD parameters and radar reflectivity were established. These relationships were then applied to estimate the rain rates from NEXRAD cloud-base radar reflectivity and were compared to the surface rain rate measurements. The main conclusions can be summarized as follows:

1. The Exponential function can capture most of the aircraft in situ measured DSD shape information except for some of the large drops, indicating that the approximation of the Gamma function by an Exponential function with $\mu_T = 0$ is valid and reasonable.
2. Comparing the Gamma shape μ_T and slope λ_T parameters from aircraft in situ measured DSDs with those derived from surface disdrometer measurements reported in Cao et al. [2008] and Cao and Zhang [2009], the ranges of overlapping μ_T and λ_T values are limited but have similar trends. Similar μ_T - λ_T relationships with different ranges from two independent platforms with different elevations may represent the real nature of the DSDs in clouds and at the surface. It is helpful to study changes in the DSD from clouds to precipitation using a combination of aircraft in situ measurements in clouds and disdrometer measurements at the surface.
3. By applying the N_{0E} - λ_E relationship to the definition of radar reflectivity factor Z_e , the rain rate can be retrieved from the NEXRAD cloud-base observed Z_e values. The averaged SR rain rate retrieved from this study is almost identical to the surface disdrometer/tipping-bucket measurements, while the NEXRAD Q2 precipitation is twice as large. These comparisons indicate that the new DSD parameterization scheme is

robust, while the Q2 SR precipitation estimation based on Marshall-Palmer Z - R relationship, where a constant DSD intercept parameter (N_{0E}) was assumed, needs to be revised for heavy precipitation.

4. Further evaluation of the Marshall-Palmer power-law Z - R relationship and the Z - R relationship based on the new DSD parameterization scheme was conducted using an independent data set from a total of 17 APU (Automatic Parsivel Unit) sites for the duration of the MC3E experiment. Comparisons show that the differences between the rain rates calculated using the Marshall-Palmer Z - R relationship and retrieved from this study are indistinguishable for $Z_e < 20$ dBZ, but the differences start to increase with increased Z_e values for $Z_e > 20$ dBZ. The major reason for the discrepancy is that the power-law Z - R relationship's linear relationship on a logarithmic scale does not represent the actual nonlinear relationship exhibited by the APU observations, while the downward curvature feature can be fully captured by the Z - R relationship developed in this study.

The excellent agreement between the retrieved rain rates from this study and the surface rain rate measurements has revealed that the DSD retrieval algorithm developed in this study is more advanced than the constant N_{0E} assumption commonly used in power-law Z - R relationship. Application of the N_{0E} - λ_E relationship may shed light on the need for the development of a regional in-cloud DSD product and thereby more accurate precipitation estimation, from radar reflectivity. This new DSD parameterization scheme and its application for precipitation estimation will also benefit the DCS modeling and forecasting communities, to whom the validation fields of in-cloud DSD and surface precipitation are needed, especially for the simulations of field campaigns before 2013 when the dual-polarization radar products were not available. It is worthwhile to note that the specific N_{0E} - λ_E relationship was obtained for the MC3E campaign, and adjustment of this relationship is necessary for different precipitation types, locations, and climatology, using observations. For precipitation estimation, the calculated rain rate could also be slightly impacted by the choice of the $V(D)$ relationship and DSD bin scheme.

For the convective core precipitation retrieval and cloud microphysical properties, the power-law Z - R relationships based on the assumption of constant N_{0E} seem more problematic due to the well-known N_{0E} jump issue [Waldvogel, 1974] caused by drastic environmental changes associated with updrafts in the microscale. Future analyses in this series will report on a more detailed DSD parameterization scheme using surface disdrometer measurements, focusing on the DCS convective cores during MC3E. Taking advantage of the improved DSD parameterization schemes for different regions of DCSs, the overarching goal of this paper series is to provide regional surface precipitation estimation and in-cloud DSD data products for evaluating the modeled cloud and precipitation properties.

Table A1. Aircraft Probes' Diameter and Width for Each Bin Used in SR Rain Rate Calculation

Diameter (μm)	Bin Width (μm)
120	30
165	60
225	60
285	60
345	60
405	60
465	60
522.5	55
600	100
700	100
800	100
900	100
1100	200
1300	200
1500	200
1700	200
2000	400
2400	400
2800	400
3200	400
3600	400
4000	400

Table B1. Summary of 17 NASA GPM GV Automatic Parsivel Unit (APU) Measurements

	Location (Longitude, Latitude)	Precipitation Amount Detectability (mm h ⁻¹)	DSD Observations	Temporal Resolution	Data Source
APU	−97.472, 36.608 (APU01)	0.01	32 size bins 0.06 to 25.2 mm	1 min	ftp://gpm.nsstc.nasa.gov/ gpm_validation/mc3e/ disdrometers_and_gauges/parsivel/ data/
	−97.506, 36.608 (APU02)				
	−97.499, 36.633 (APU03)				
	−97.466, 36.608 (APU04)				
	−97.517, 36.635 (APU05)				
	−97.543, 36.637 (APU06)				
	−97.552, 36.615 (APU07)				
	−97.516, 36.615 (APU08)				
	−97.489, 36.594 (APU09)				
	−97.507, 36.594 (APU10)				
	−97.499, 36.578 (APU11)				
	−97.480, 36.569 (APU12)				
	−97.463, 36.579 (APU13)				
	−97.426, 36.600 (APU14)				
	−97.427, 36.578 (APU15)				
	−97.453, 36.564 (APU16)				
	−97.485, 36.604 (APU17)				

Appendix A

For SR rain rate calculation, a full spectrum of raindrop size distribution (DSD) was constructed from 120 μm to 4000 μm through a combination of 2DC (120 to 900 μm) and HVPS (900 to 4000 μm) data sets. The central diameter and bin width for each bin are shown in Table A1.

Appendix B

In order to assess different precipitation retrieval methods, additional surface rain rate measurements from a total of 17 APU (Automatic Parsivel Unit) sites for the entire MC3E campaign (from 22 April to 6 June 2011) were collected and processed as an independent validation data set. A brief summary of APU stations is listed in Table B1.

Acknowledgments

The data were obtained from the Atmospheric Radiation Measurement (ARM) Program sponsored by the U.S. Department of Energy (DOE) Office of Energy Research, Office of Health and Environmental Research, and Environmental Sciences Division. This study was primarily supported by DOE ASR project at University of North Dakota with award number DE-SC0008468 and the NOAA R20 project at University of North Dakota project under grant NA15NWS4680004. Andrew J. Heymsfield was supported by NASA GPM Project NNX13AH73G at NCAR. Special thanks to Jensen, PI of MC3E, and UND flight crew who calibrated and operated all airborne instruments and processed the Citation II raw data during MC3E experiment. Special thanks to Aaron Bansemmer who provided OAP processing algorithm. We would like to thank Logan for proofreading of the manuscript and O'Brien for particle image interpretation. The data used in this study were downloaded through ftp://gpm.nsstc.nasa.gov/gpm_validation/mc3e/ on April 2015, and the processed cloud microphysical properties through aircraft in situ measurements during MC3E can be obtained from Xiquan Dong (dong@aero.und.edu).

References

- Baldwin, M. E., and K. E. Mitchell (1998), Progress on the NCEP hourly multi-sensor U.S. precipitation analysis for operations and GCIP research 2nd Symposium on Integrated Observing Systems, 78th AMS Annual Meeting, 10–11, Phoenix, Ariz.
- Barros, A. P., O. P. Prat, P. Shrestha, F. Y. Testik, and L. F. Bliven (2008), Revisiting Low and List (1982): Evaluation of raindrop collision parameterizations using laboratory observations and modeling, *J. Atmos. Sci.*, *65*, 2983–2993, doi:10.1175/2008JAS2630.1.
- Barthazy, E., W. Henrich, and A. Waldvogel (1998), Size distribution of hydrometeors through the melting layer, *Atmos. Res.*, *47–48*, 193–208.
- Boudala, F. S., G. A. Isaac, and D. Hudak (2006), Ice water content and precipitation rate as a function of equivalent radar reflectivity and temperature based on in situ observations, *J. Geophys. Res.*, *111*, D11202, doi:10.1029/2005JD006499.
- Brandes, E. A., G. Zhang, and J. Vivekanandan (2004), Drop size distribution retrieval with polarimetric radar: Model and application, *J. Appl. Meteorol.*, *43*, 461–475, doi:10.1175/1520-0450(2004)043<0461:DSDRWP>2.0.CO;2.
- Bringi, V. N., G. Huang, V. Chandrasekar, and E. Gorgucci (2002), A methodology for estimating the parameters of a gamma raindrop size distribution model from polarimetric radar data: Application to a squall-line event from the TRMM/Brazil campaign, *J. Atmos. Oceanic Technol.*, *19*(5), 633–645.
- Brock, F. V., K. C. Crawford, R. L. Elliott, G. W. Cuperus, S. J. Stadler, H. L. Johnson, and M. D. Eilts (1995), The Oklahoma Mesonet: A technical overview, *J. Atmos. Oceanic Technol.*, *12*, 5–19, doi:10.1175/1520-0426(1995)012<0005:TOMATO>2.0.CO;2.
- Cao, Q., and G. Zhang (2009), Errors in estimating raindrop size distribution parameters employing disdrometer and simulated raindrop spectra, *J. Appl. Meteorol. Climatol.*, *48*, 406–425, doi:10.1175/2008JAMC2026.1.
- Cao, Q., G. Zhang, E. Brandes, T. Schuur, A. Ryzhkov, and K. Ikeda (2008), Analysis of video disdrometer and polarimetric radar data to characterize rain microphysics in Oklahoma, *J. Appl. Meteorol. Climatol.*, *47*, 2238–2255, doi:10.1175/2008JAMC1732.1.
- Chandrasekar, V., W. A. Cooper, and V. N. Bringi (1988), Axis ratios and oscillations of raindrops, *J. Atmos. Sci.*, *45*, 1323–1333, doi:10.1175/1520-0469(1988)045<1323:ARAOOR>2.0.CO;2.
- Chen, S., J. J. Gourley, Y. Hong, P. E. Kirstetter, J. Zhang, K. Howard, Z. L. Flamig, J. Hu, and Y. Qi (2013), Evaluation and uncertainty estimation of NOAA/NSSL next-generation National Mosaic Quantitative Precipitation Estimation product (Q2) over the continental United States, *J. Hydrometeorol.*, *14*, 1308–1322, doi:10.1175/JHM-D-12-0150.1.
- Clark, A. J., R. G. Bullock, T. L. Jensen, M. Xue, and F. Kong (2014), Application of object-based time-domain diagnostics for tracking precipitation systems in convection-allowing models, *Weather Forecasting*, *29*, 517–542, doi:10.1175/WAF-D-13-00098.1.

- Dong, X., T. P. Ackerman, and E. E. Clothiaux (1998), Parameterizations of microphysical and radiative properties of boundary layer stratus from ground-based measurements, *J. Geophys. Res.*, *102*, 31,681–31,693, doi:10.1029/1998JD200047.
- Dong, X., P. Minnis, G. G. Mace, W. L. Smith Jr., M. Poellot, R. Marchand, and A. D. Rapp (2002), Comparison of stratus cloud properties deduced from surface, GOES, and aircraft data during the March 2000 ARM Cloud IOP, *J. Atmos. Sci.*, *59*, 3265–3284.
- Ecklund, W. L., C. R. Williams, P. E. Johnston, and K. S. Gage (1999), A 3-GHz profiler for precipitating cloud studies, *J. Atmos. Oceanic Technol.*, *16*, 309–322.
- Emersic, C., and P. J. Connolly (2011), The breakup of levitating water drops observed with high speed camera, *Atmos. Chem. Phys.*, *11*, 10,205–10,218, doi:10.5194/acp-11-10205-2011.
- Fan, J., Y.-C. Liu, K.-M. Xu, K. North, S. Collis, X. Dong, G. J. Zhang, Q. Chen, P. Kollias, and S. J. Ghan (2015), Improving representation of convective transport for scale-aware parameterization: 1. Convection and cloud properties simulated with spectral bin and bulk microphysics, *J. Geophys. Res. Atmos.*, *120*, 3485–3509, doi:10.1002/2014JD022142.
- Feng, Z., X. Dong, B. Xi, C. Schumacher, P. Minnis, and M. Khaiyer (2011), Top-of-atmosphere radiation budget of convective core/stratiform rain and anvils from deep convective systems, *J. Geophys. Res.*, *116*, D23202, doi:10.1029/2011JD016451.
- Feng, Z., X. Dong, B. Xi, S. A. McFarlane, A. Kennedy, B. Lin, and P. Minnis (2012), Life cycle of midlatitude deep convective systems in a Lagrangian framework, *J. Geophys. Res.*, *117*, D23201, doi:10.1029/2012JD018362.
- Field, P. R., A. J. Heymsfield, and A. Bansemmer (2006), Shattering and particle interarrival times measured by optical array probes in ice clouds, *J. Atmos. Oceanic Technol.*, *23*, 1357–1371, doi:10.1175/JTECH1922.1.
- Fujiyoshi, Y. (1986), Melting snowflakes, *J. Atmos. Sci.*, *43*, 307–311, doi:10.1175/1520-0469(1986)043<0307:MS>2.0.CO;2.
- Futyan, J. M., and A. D. Del Genio (2007), Deep convective system evolution over Africa and the tropical Atlantic, *J. Clim.*, *20*, 5041–5060, doi:10.1175/JCLI4297.1.
- Giannandrea, S. E., S. Collis, A. K. Theisen, and A. Tokay (2014), Precipitation estimation from the ARM distributed radar network during the MC3E campaign, *J. Appl. Meteorol. Climatol.*, *53*(9), 2130–2147, doi:10.1175/JAMC-D-13-0321.1.
- Gunn, R., and G. D. Kinzer (1949), The terminal velocity of fall for water drops in stagnant air, *J. Meteorol.*, *6*, 243–248, doi:10.1175/1520-0469(1949)006<0243:TTVOFF>2.0.CO;2.
- Heymsfield, A. J., and J. L. Parrish (1978), A computational technique for increasing the effective sampling volume of the PMS two-dimensional particle size spectrometer, *J. Appl. Meteorol.*, *17*, 1566–1572.
- Heymsfield, A. J., C. Schmitt, A. Bansemmer, and C. H. Twohy (2010), Improved representation of ice particle masses based on observations in natural clouds, *J. Atmos. Sci.*, *67*, 3303–3318, doi:10.1175/2010JAS3507.1.
- Heymsfield, A. J., A. Bansemmer, M. R. Poellot, and N. Wood (2015), Observations of ice microphysics through the melting layer, *J. Atmos. Sci.*, *72*, 2902–2928, doi:10.1175/JAS-D-14-0363.1.
- Heymsfield, G. M., and R. Fulton (1988), Comparison of high-altitude remote aircraft measurements with the radar structure of an Oklahoma thunderstorm: Implications for precipitation estimation from space, *Mon. Weather Rev.*, *116*, 1157–1174, doi:10.1175/1520-0493(1988)116<1157:COHARA>2.0.CO;2.
- Homeyer, C. R. (2014), Formation of the enhanced-V infrared cloud top feature from high-resolution three-dimensional radar observations, *J. Atmos. Sci.*, *71*, 332–348, doi:10.1175/JAS-D-13-079.1.
- Homeyer, C. R., and M. R. Kumjian (2015), Microphysical characteristics of overshooting convection from polarimetric radar observations, *J. Atmos. Sci.*, *72*, 870–891, doi:10.1175/JAS-D-13-0388.1.
- Iguchi, T., T. Kozu, R. Meneghini, J. Awaka, and K. Okamoto (2000), Rain-profiling algorithm for the TRMM precipitation radar, *J. Appl. Meteorol.*, *39*, 2038–2052, doi:10.1175/1520-0450(2001)040<2038:RPAFTT>2.0.CO;2.
- Jameson, A. R., and K. V. Beard (1982), Raindrop axial ratios, *J. Appl. Meteorol.*, *21*, 257–259, doi:10.1175/1520-0450(1982)021<0257:RAR>2.0.CO;2.
- Jeffrey, A., and H. Dai (2008), *Handbook of Mathematical Formulas*, 4th ed., pp. 234–235, Academic Press, Cambridge, Mass.
- Jensen, M., et al. (2015), The Midlatitude Continental Convective Clouds Experiment (MC3E), *Bull. Am. Meteorol. Soc.*, doi:10.1175/BAMS-D-14-00228.1.
- Khain, A. P., K. D. Beheng, A. Heymsfield, A. Korolev, S. O. Krichak, Z. Levin, M. Pinsky, V. Phillips, T. Prabhakaran, and A. Teller (2015), Representation of microphysical processes in cloud-resolving models: Spectral (bin) microphysics versus bulk parameterization, *Rev. Geophys.*, *53*, 247–322, doi:10.1002/2014RG000468.
- Korolev, A., and G. Isaac (2003), Roundness and aspect ratio of particles in ice clouds, *J. Atmos. Sci.*, *60*, 1795–1808, doi:10.1175/1520-0469(2003)060<1795:RAAROP>2.0.CO;2.
- Korolev, A. V. (2007), Reconstruction of the sizes of spherical particles from their shadow images. Part I: Theoretical considerations, *J. Atmos. Oceanic Technol.*, *24*, 376–389, doi:10.1175/JTECH1980.1.
- Korolev, A. V., J. W. Strapp, G. A. Isaac, and A. N. Nevzorov (1998), The Nevzorov airborne hot-wire LWC-TWC probe: Principles of operation and performance characteristics, *J. Atmos. Oceanic Technol.*, *15*, 1495–1510.
- Kumjian, M. R. (2013), Principles and applications of dual-polarization weather radar. Part I: Description of the polarimetric radar variables, *J. Oper. Meteorol.*, *1*(19), 226–242.
- Kumjian, M. R., and O. P. Prat (2014), The impact of raindrop collisional processes on the polarimetric radar variables, *J. Atmos. Sci.*, *71*, 3052–3067, doi:10.1175/JAS-D-13-0357.1.
- Lee, G. W., I. Zawadzki, W. Szyrmer, D. Sempere-Torres, and R. Uijlenhoet (2004), A general approach to double-moment normalization of drop size distributions, *J. Appl. Meteorol.*, *43*(2), 264–281, doi:10.1175/1520-0450(2004)043<0264:AGATDN>2.0.CO;2.
- Liao, L., R. Meneghini, and A. Tokay (2014), Uncertainties of GPM DPR rain estimates caused by DSD parameterizations, *J. Appl. Meteorol. Climatol.*, *53*, 2524–2537, doi:10.1175/JAMC-D-14-0003.1.
- Lin, Y., and K. E. Mitchell (2005), The NCEP stage II/IV hourly precipitation analyses: Development and applications paper 1.2 presented at 19th Conference on Hydrology, Am. Meteorol. Soc., San Diego, Calif., 9–13 Jan.
- Liu, C., E. Zipser, and S. W. Nesbitt (2007), Global distribution of tropical deep convection: Different perspectives from TRMM infrared and radar data, *J. Clim.*, *20*, 489–503, doi:10.1175/JCLI4023.1.
- Low, T. B., and R. List (1982a), Collision, coalescence and breakup of raindrops. Part I: Experimentally established coalescence efficiencies and fragment size distributions in breakup, *J. Atmos. Sci.*, *39*, 1591–1606.
- Low, T. B., and R. List (1982b), Collision, coalescence and breakup of raindrops. Part II: Parameterizations of fragment size distributions, *J. Atmos. Sci.*, *39*, 1607–1618.
- Mace, G. G., A. J. Heymsfield, and M. R. Poellot (2002), On retrieving the microphysical properties of cirrus clouds using the moments of the millimeter-wavelength Doppler spectrum, *J. Geophys. Res.*, *107*(D24), 4815, doi:10.1029/2001JD001308.
- Marshall, J. S., and W. M. Palmer (1948), The distribution of raindrops with size, *J. Meteorol.*, *5*, 165–166.

- McFarquhar, G. M. (2004a), A new representation of collision-induced breakup of raindrops and its implications for the shapes of raindrop size distributions, *J. Atmos. Sci.*, *61*, 777–794, doi:10.1175/1520-0469(2004)061<0777:ANROCB>2.0.CO;2.
- McFarquhar, G. M. (2004b), The effect of raindrop clustering on collision-induced break-up of raindrops, *Q. J. R. Meteorol. Soc.*, *130*, 2169–2190, doi:10.1256/qj.03.98.
- McFarquhar, G. M., and A. J. Heymsfield (1996), Microphysical characteristics of three anvils sampled during the Central Equatorial Pacific Experiment, *J. Atmos. Sci.*, *53*, 2401–2423, doi:10.1175/1520-0469(1996)053<2401:MCOTAS>2.0.CO;2.
- McFarquhar, G. M., and R. List (1991a), The evolution of three-peak raindrop size distributions in one-dimensional shaft models. Part II: Multiple pulse rain, *J. Atmos. Sci.*, *48*, 1587–1595, doi:10.1175/1520-0469(1991)048<1587:TEOTPR>2.0.CO;2.
- McFarquhar, G. M., and R. List (1991b), The raindrop mean free path and collision rate dependence on rainrate for three-peak equilibrium and Marshall-Palmer distributions, *J. Atmos. Sci.*, *48*, 1999–2003, doi:10.1175/1520-0469(1991)048<1999:TRMFPA>2.0.CO;2.
- McFarquhar, G. M., G. Zhang, M. R. Poellot, G. L. Kok, R. McCoy, T. Tooman, A. Fridlind, and A. J. Heymsfield (2007), Ice properties of single-layer stratocumulus during the Mixed-Phase Arctic Cloud Experiment: 1. Observations, *J. Geophys. Res.*, *112*, D24201, doi:10.1029/2007JD008633.
- McFarquhar, G., T. L. Hsieh, M. Freer, J. Mascio, and B. Jewett (2015), The characterization of ice hydrometeor gamma size distributions as volumes in $N_0-\Lambda T-\mu$ phase space: Implications for microphysical process modeling, *J. Atmos. Sci.*, *72*, 892–909.
- Nelson, B. R., D.-J. Seo, and D. Kim (2010), Multisensor precipitation reanalysis, *J. Hydrometeorol.*, *11*, 666–682, doi:10.1175/2010JHM1210.1.
- Oraltay, R. G., and J. Hallett (2005), The melting layer: A laboratory investigation of ice particle melt and evaporation near 0°C, *J. Appl. Meteorol.*, *44*, 206–220, doi:10.1175/JAM2194.1.
- Patade, S., T. V. Prabha, D. Axisa, K. Gayatri, and A. Heymsfield (2015), Particle size distribution properties in mixed-phase monsoon clouds from in situ measurements during CAIPEEX, *J. Geophys. Res. Atmos.*, *120*, 10,418–10,440, doi:10.1002/2015JD023375.
- Press, W. H., S. A. Teukolsky, W. T. Vetterling, and B. P. Flannery (1992), Numerical recipes in FORTRAN, in *The Art of Scientific Computing*, 2nd ed., pp. 678–683, Cambridge Univ. Press, New York.
- Pruppacher, H. R., and J. D. Klett (1996), *Microphysics of Clouds and Precipitation*, 2nd ed., pp. 798, Kluwer Acad., Dordrecht, Netherlands.
- Rosenfeld, D., D. B. Wolff, and D. Atlas (1993), General probability-matched relations between radar reflectivity and rain rate, *J. Appl. Meteorol.*, *32*, 50–72.
- Ryzhkov, A. V. (2007), The impact of beam broadening on the quality of radar polarimetric data, *J. Atmos. Oceanic Technol.*, *24*, 729–744.
- Ryzhkov, A. V., T. J. Schuur, D. W. Burgess, P. L. Heinselman, S. E. Giangrande, and D. S. Zrnić (2005a), The joint polarization experiment: Polarimetric rainfall measurements and hydrometeor classification, *Bull. Am. Meteorol. Soc.*, *86*, 809–824, doi:10.1175/BAMS-86-6-809.
- Ryzhkov, A. V., S. E. Giangrande, V. M. Melnikov, and T. J. Schuur (2005b), Calibration issues of dual-polarization radar measurements, *J. Atmos. Oceanic Technol.*, *22*, 1138–1155.
- Schlottke, J. W., W. Straub, K. D. Beheng, H. Goma, and B. Weigand (2010), Numerical investigation of collision-induced breakup of raindrops. Part I: Methodology and dependencies on collision and eccentricity, *J. Atmos. Sci.*, *67*, 557–575, doi:10.1175/2009JAS3174.1.
- Schumacher, C., and R. A. Houze (2003), Stratiform rain in the tropics as seen by the TRMM precipitation radar, *J. Clim.*, *16*, 1739–1756, doi:10.1175/1520-0442(2003)016<1739:SRITTA>2.0.CO;2.
- Seifert, A., A. Khain, and U. Blahak (2005), Possible effects of collisional breakup on mixed-phase deep convection simulated by a spectral (bin) cloud model, *J. Atmos. Sci.*, *62*(6), 1917–1931, doi:10.1175/JAS3432.1.
- Sempere-Torres, D., J. M. Porrà, and J.-D. Creutin (1994), A general formulation for raindrop size distribution, *J. Appl. Meteorol.*, *33*, 1494–1502.
- Sempere-Torres, D., J. M. Porrà, and J.-D. Creutin (1998), Experimental evidence of a general description for raindrop size distribution properties, *J. Geophys. Res.*, *103*, 1785–1797, doi:10.1029/97JD02065.
- Sheppard, B. E., and P. I. Joe (1994), Comparison of raindrop size distribution measurements by a Joss-Waldvogel Disdrometer, a PMS 2DG Spectrometer, and a POSS Doppler radar, *J. Atmos. Oceanic Technol.*, *11*, 874–887, doi:10.1175/1520-0426(1994)011<0874:CORSMD>2.0.CO;2.
- Steiner, M., R. A. Houze, and S. E. Yuter (1995), Climatological characterization of three-dimensional storm structure from operational radar and rain gauge data, *J. Appl. Meteorol.*, *34*, 1978–2007, doi:10.1175/1520-0450(1995)034<1978:CCOTDS>2.0.CO;2.
- Stenz, R., X. Dong, B. Xi, and R. J. Kuligowski (2014), Assessment of SCA-MPR and NEXRAD Q2 precipitation estimates using Oklahoma Mesonet observations, *J. Hydrometeorol.*, *15*, 2484–2500, doi:10.1175/JHM-D-13-0199.1.
- Stenz, R., X. Dong, B. Xi, Z. Feng, and R. J. Kuligowski (2015), Improving satellite quantitative precipitation estimates using GOES-retrieved cloud optical depth, *J. Hydrometeorol.*, *15*, 2484–2500, doi:10.1175/JHM-D-15-0057.1.
- Szumowski, M. J., R. M. Rauber, H. T. Ochs III, and L. J. Miller (1997), The microphysical structure and evolution of Hawaiian rainband clouds. Part I: Radar observations of rainbands containing high reflectivity cores, *J. Atmos. Sci.*, *54*, 369–385, doi:10.1175/1520-0469(1997)054<0369:TMSAEO>2.0.CO;2.
- Szumowski, M. J., R. M. Rauber, H. T. Ochs III, and K. V. Beard (1998), The microphysical structure and evolution of Hawaiian rainband clouds. Part II: Aircraft measurements within rainbands containing high reflectivity cores, *J. Atmos. Sci.*, *55*, 208–226, doi:10.1175/1520-0469(1998)055<0208:TMSAEO>2.0.CO;2.
- Testud, J., S. Oury, R. A. Black, P. Amayenc, and X. Dou (2001), The concept of “normalized” distribution to describe rain-drop spectra: A tool for cloud physics and remote sensing, *J. Appl. Meteorol.*, *40*, 1118–1140.
- Tian, L., G. M. Heymsfield, L. Li, and R. C. Srivastava (2007), Properties of light stratiform rain derived from 10- and 94-GHz airborne Doppler radars measurements, *J. Geophys. Res.*, *112*, D11211, doi:10.1029/2006JD008144.
- Tokay, A., and D. A. Short (1996), Evidence from tropical raindrop spectra of the origin of rain from stratiform versus convective clouds, *J. Appl. Meteorol.*, *35*, 355–371, doi:10.1175/1520-0450(1996)035<0355:EFTRSO>2.0.CO;2.
- Tokay, A., A. Kruger, and W. Krajewski (2001), Comparison of drop size distribution measurements by impact and optical disdrometers, *J. Appl. Meteorol.*, *40*, 2083–2097, doi:10.1175/1520-0450(2001)040<2083:CODSDM>2.0.CO;2.
- Tromel, S., A. Ryzhkov, P. Zhang, and C. Simmer (2014), Investigations of backscatter differential phase in the melting layer, *J. Appl. Meteorol. Climatol.*, *53*, 2344–2359, doi:10.1175/JAMC-D-14-0050.1.
- Ulbrich, C. W. (1983), Natural variations in the analytical form of the raindrop size distribution, *J. Clim. Appl. Meteorol.*, *22*, 1764–1775, doi:10.1175/1520-0450(1983)022<1764:NVITAF>2.0.CO;2.
- Waldvogel, A. (1974), The N0 jump of raindrop spectra, *J. Atmos. Sci.*, *31*, 1067–1078, doi:10.1175/1520-0469(1974)031<1067:TJORS>2.0.CO;2.
- Wang, J., X. Dong, and B. Xi (2015), Investigation of ice cloud microphysical properties of DCSs using aircraft in situ measurements during MC3E over the ARM SGP site, *J. Geophys. Res. Atmos.*, *120*, 3533–3552, doi:10.1002/2014JD022795.
- Williams, C. R., et al. (2014), Describing the shape of raindrop size distributions using uncorrelated raindrop mass spectrum parameters, *J. Appl. Meteorol. Climatol.*, *53*, 1282–1296, doi:10.1175/JAMC-D-13-076.1.

- Xu, W. (2013), Precipitation and convective characteristics of summer deep convection over East Asia observed by TRMM, *Mon. Weather Rev.*, 141, 1577–1592, doi:10.1175/MWR-D-12-00177.1.
- Zhang, G., J. Vivekanandan, and E. A. Brandes (2001), A method for estimating rain rate and drop size distribution from polarimetric radar measurements, *IEEE Trans. Geosci. Remote Sens.*, 39, 830–841.
- Zhang, G., J. Vivekanandan, E. A. Brandes, R. Meneghini, and T. Kozu (2003), The shape-slope relation in observed gamma raindrop size distributions: Statistical error or useful information?, *J. Atmos. Oceanic Technol.*, 20, 1106–1119, doi:10.1175/1520-0426(2003)020<1106:TSRIOG>2.0.CO;2.
- Zhang, J., et al. (2011), National Mosaic and Multi-Sensor QPE (NMQ) system: Description, results, and future plans, *Bull. Am. Meteorol. Soc.*, 92, 1321–1338, doi:10.1175/2011BAMS-D-11-00047.1.
- Zhang, J., et al. (2015), Multi-Radar Multi-Sensor (MRMS) quantitative precipitation estimation: Initial operating capabilities, *Bull. Am. Meteorol. Soc.*, 97, 621–638, doi:10.1175/BAMS-D-14-00174.1.
- Zrnica, D. S., and A. V. Ryzhkov (1999), Polarimetry for weather surveillance radars, *Bull. Am. Meteorol. Soc.*, 80, 389–406.